Title
Measurement of CP-violating asymmetries in B0→(ρπ)0 using a time-dependent Dalitz plot analysis

Journal
Physical Review D - Particles, Fields, Gravitation and Cosmology, 76(1)

ISSN
1550-7998

Authors
Aubert, B
Bona, M
Boutigny, D
et al.

Publication Date
2007-07-18

DOI
10.1103/PhysRevD.76.012004

Measurement of CP-violating asymmetries in $B^0 \to (\rho\pi)^0$ using a time-dependent Dalitz plot analysis

B. Aubert,[1] M. Bona,[1] D. Boutigny,[1] Y. Karyotakis,[1] J. P. Lees,[1] V. Poireau,[1] X. Prudent,[1] V. Tisserand,[1] A. Zghiche,[1] J. Garra Tico,[2] E. Grauges,[2] L. Lopez,[3] A. Palano,[3] G. Eigen,[4] I. Ofte,[4] B. Stugu,[4] L. Sun,[4] G. S. Abrams,[5] M. Battaglia,[5] D. N. Brown,[5] J. Button-Shafer,[5] R. N. Cahn,[5] Y. Groysman,[5] R. G. Jacobsen,[5] J. A. Kadyk,[5] L. T. Kerth,[5] Yu. G. Kolomensky,[5] G. Kukartsev,[5] D. Lopes Pegna,[5] G. Lynch,[5] L. M. Mir,[5] T. J. Orimoto,[5] M. Pripstein,[5] N. A. Roe,[5] M. T. Ronan,[5,*] K. Tackmann,[5] W. A. Wenzel,[5] P. del Amo Sanchez,[6] C. M. Hawkes,[6] A. T. Watson,[6] T. Held,[7] H. Koch,[7] B. Lewandowski,[7] M. Pelizaeus,[7] T. Schroeder,[7] M. Steinke,[7] J. T. Boyd,[8] J. P. Burke,[8] W. N. Cottingham,[8] D. Walker,[8] D. J. Asgeirsson,[9] T. Cuhadar-Donszelmann,[9] B. G. Fulsom,[9] C. Hearty,[9] N. S. Knecht,[9] T. S. Mattison,[9] J. A. McKenna,[9] A. Khan,[10] M. Saleem,[10] L. Teodorescu,[10] V. E. Blinov,[11] A. D. Bukin,[11] V. P. Druzhinin,[11] V. B. Golubev,[11] A. P. Onuchin,[11] S. I. Serednyakov,[11] Yu. I. Skovpen,[11] E. P. Solodov,[11] K. Yu. Todyshev,[11] M. Bondioli,[12] M. Bruinsma,[12] S. Curry,[12] I. Eschrich,[12] D. Kirkby,[12] A. J. Lankford,[12] P. Lund,[12] M. Mandelkern,[12] E. C. Martin,[12] D. P. Stoker,[12] S. Abachi,[13] C. Buchanan,[13] S. D. Foulkes,[14] J. W. Gary,[14] F. Liu,[14] O. Long,[14] B. C. Shen,[14] L. Zhang,[14] H. P. Paar,[15] S. Rahatlou,[15] V. Sharma,[15] J. W. Berryhill,[16] C. Campagnari,[16] A. Cunha,[16] B. Dahmes,[16] T. M. Hong,[16] D. Kovalskyi,[16] J. D. Richman,[16] T. W. Beck,[17] A. M. Eisner,[17] C. J. Flacco,[17] C. A. Heusch,[17] J. Kroseberg,[17] W. S. Lockman,[17] T. Schalk,[17] B. A. Schumm,[17] A. Seiden,[17] D. C. Williams,[17] M. G. Wilson,[17] L. O. Winstrom,[17] E. Chen,[18] C. H. Cheng,[18] A. Dvoretskii,[18] F. Fang,[18] D. G. Hitlin,[18] I. Narsky,[18] T. Piatenko,[18] F. C. Porter,[18] G. Mancinelli,[19] B. T. Meadows,[19] K. Mishra,[19] M. D. Sokoloff,[19] F. Blanc,[20] P. C. Bloom,[20] S. Chen,[20] W. T. Ford,[20] J. F. Hirschauer,[20] A. Kreisel,[20] M. Nagel,[20] U. Nauenberg,[20] A. Olivas,[20] J. G. Smith,[20] K. A. Ulmer,[20] S. R. Wagner,[20] J. Zhang,[20] A. Chen,[21] E. A. Eckhart,[21] A. Soffer,[21] W. H. Toki,[21] R. J. Wilson,[21] F. Winklmeier,[21] Q. Zeng,[21] D. D. Altenburg,[22] E. Feltresi,[22] A. Hauke,[22] H. Jasper,[22] J. Merkel,[22] A. Petzold,[22] B. Spaan,[22] K. Wacker,[22] T. Brandt,[23] V. Klose,[23] H. M. Lacker,[23] W. F. Mader,[23] R. Nogowski,[23] J. Schubert,[23] K. R. Schubert,[23] R. Schwierz,[23] J. E. Sundermann,[23] A. Volk,[23] D. Bernard,[24] G. R. Bonneaud,[24] E. Latour,[24] Ch. Thiebaux,[24] M. Verderi,[24] P. J. Clark,[25] W. Gradl,[25] F. Muheim,[25] S. Playfer,[25] A. I. Robertson,[25] Y. Xie,[25] M. Andreotti,[26] D. Bettoni,[26] C. Bozzi,[26] R. Calabrese,[26] A. Cecchi,[26] G. Cibinetto,[26] P. Franchini,[26] E. Luppi,[26] M. Negrini,[26] A. Petrella,[26] L. Piemontese,[26] E. Prencipe,[26] V. Santoro,[26] F. Anulli,[27] R. Baldini-Ferroli,[27] A. Calcaterra,[27] R. de Sangro,[27] G. Finocchiaro,[27] S. Pacetti,[27] P. Patteri,[27] I. M. Peruzzi,[27,†] M. Piccolo,[27] M. Rama,[27] A. Zallo,[27] A. Buzzo,[28] R. Contri,[28] M. Lo Vetere,[28] M. M. Macri,[28] M. R. Monge,[28] S. Passaggio,[28] C. Patrignani,[28] E. Robutti,[28] A. Santroni,[28] S. Tosi,[28] K. S. Chaisanguanthum,[29] M. Morii,[29] J. Wu,[29] R. S. Dubitzky,[30] J. Marks,[30] S. Schenk,[30] U. Uwer,[30] D. J. Bard,[31] P. D. Dauncey,[31] R. L. Flack,[31] J. A. Nash,[31] M. B. Nikolich,[31] W. Panduro Vazquez,[31] P. K. Behera,[32] X. Chai,[32] M. J. Charles,[32] U. Mallik,[32] N. T. Meyer,[32] V. Ziegler,[32] J. Cochran,[33] H. B. Crawley,[33] L. Dong,[33] V. Eyges,[33] W. T. Meyer,[33] S. Prell,[33] E. I. Rosenberg,[33] A. E. Rubin,[33] A. V. Gritsan,[34] C. K. Lae,[34] A. G. Denig,[35] M. Fritsch,[35] G. Schott,[35] N. Arnaud,[36] J. Béquilleux,[36] M. Davier,[36] G. Grosdidier,[36] A. Höcker,[36] V. Lepeltier,[36] F. Le Diberder,[36] A. M. Lutz,[36] S. Pruvot,[36] S. Rodier,[36] P. Roudeau,[36] M. H. Schune,[36] J. Serrano,[36] V. Sordini,[36] A. Stocchi,[36] W. F. Wang,[36] G. Wormser,[36] D. J. Lange,[37] D. M. Wright,[37] C. A. Chavez,[38] I. J. Forster,[38] J. R. Fry,[38] E. Gabathuler,[38] R. Gamet,[38] D. E. Hutchcroft,[38] D. J. Payne,[38] K. C. Schofield,[38] C. Touramanis,[38] A. J. Bevan,[39] K. A. George,[39] F. Di Lodovico,[39] W. Menges,[39] R. Sacco, G. Cowan,[40] H. U. Flaecher,[40] D. A. Hopkins,[40] P. S. Jackson,[40] T. R. McMahon,[40] F. Salvatore,[40] A. C. Wren,[40] D. N. Brown,[41] C. L. Davis,[41] J. Allison,[42] N. R. Barlow,[42] R. J. Barlow,[42] Y. M. Chia,[42] C. L. Edgar,[42] G. D. Lafferty,[42] T. J. West,[42] J. I. Yi,[42] J. Anderson,[42] C. Chen,[43] A. Jawahery,[43] D. A. Roberts,[43] G. Simi,[43] J. M. Tuggle,[43] G. Blaylock,[44] C. Dallapiccola,[44] S. S. Hertzbach,[44] X. Li,[44] T. B. Moore,[44] E. Salvati,[44] S. Saremi,[44] R. Cowan,[45] P. H. Fisher,[45] G. Sciolla,[45] S. J. Sekula,[45] M. Spitznagel,[45] F. Taylor,[45] R. K. Yamamoto,[45] H. Kim,[46] S. E. Mclachlin,[46] P. M. Patel,[46] S. H. Robertson,[46] A. Lazzaro,[47] V. Lombardo,[47] F. Palombo,[47] J. M. Bauer,[48] L. Cremaldi,[48] V. Eschenburg,[48] R. Godang,[48] R. Kroeger,[48] D. A. Sanders,[48] D. J. Summers,[48] H. W. Zhao,[48] S. Brunet,[49] D. Côté,[49] M. Simard,[49] P. Taras,[49] F. B. Viaud,[49] H. Nicholson,[50] G. De Nardo,[51] F. Fabozzi,[51,‡] L. Lista,[51] D. Monorchio,[51] C. Sciacca,[51] M. A. Baak,[52] G. Raven,[52] H. L. Snoek,[52] C. P. Jessop,[53] J. M. LoSecco,[53] G. Benelli,[54] L. A. Corwin,[54] K. K. Gan,[54] K. Honscheid,[54] D. Hufnagel,[54] H. Kagan,[54] R. Kass,[54] J. P. Morris,[54] A. M. Rahimi,[54] J. J. Regensburger,[54] R. Ter-Antonyan,[54] Q. K. Wong,[54] N. L. Blount,[55] J. Brau,[55] R. Frey,[55] O. Igonkina,[55] J. A. Kolb,[55] M. Lu,[55] R. Rahmat,[55] N. B. Sinev,[55] D. Strom,[55] J. Strube,[55] E. Torrence,[55] N. Gagliardi,[56] A. Gaz,[56] M. Margoni,[56] M. Morandin,[56] A. Pompili,[56] M. Posocco,[56] M. Rotondo,[56] F. Simonetto,[56] R. Stroili,[56] C. Voci,[56] E. Ben-Haim,[57] H. Briand,[57] J. Chauveau,[57] P. David,[57] L. Del Buono,[57] Ch. de la Vaissière,[57] O. Hamon,[57] B. L. Hartfiel,[57] Ph. Leruste,[57] J. Malclès,[57]

J. Ocariz,[57] A. Perez,[57] L. Gladney,[58] M. Biasini,[59] R. Covarelli,[59] E. Manoni,[59] C. Angelini,[60] G. Batignani,[60] S. Bettarini,[60] G. Calderini,[60] M. Carpinelli,[60] R. Cenci,[60] F. Forti,[60] M. A. Giorgi,[60] A. Lusiani,[60] G. Marchiori,[60] M. A. Mazur,[60] M. Morganti,[60] N. Neri,[60] E. Paoloni,[60] G. Rizzo,[60] J. J. Walsh,[60] M. Haire,[61] J. Biesiada,[62] P. Elmer,[62] Y. P. Lau,[62] C. Lu,[62] J. Olsen,[62] A. J. S. Smith,[62] A. V. Telnov,[62] E. Baracchini,[63] F. Bellini,[63] G. Cavoto,[63] A. D'Orazio,[63] D. del Re,[63] E. Di Marco,[63] R. Faccini,[63] F. Ferrarotto,[63] F. Ferroni,[63] M. Gaspero,[63] P. D. Jackson,[63] L. Li Gioi,[63] M. A. Mazzoni,[63] S. Morganti,[63] G. Piredda,[63] F. Polci,[63] F. Renga,[63] C. Voena,[63] M. Ebert,[64] H. Schröder,[64] R. Waldi,[64] T. Adye,[65] G. Castelli,[65] B. Franek,[65] E. O. Olaiya,[65] S. Ricciardi,[65] W. Roethel,[65] F. F. Wilson,[65] R. Aleksan,[66] S. Emery,[66] M. Escalier,[66] A. Gaidot,[66] S. F. Ganzhur,[66] G. Hamel de Monchenault,[66] W. Kozanecki,[66] M. Legendre,[66] G. Vasseur,[66] Ch. Yèche,[66] M. Zito,[66] X. R. Chen,[67] H. Liu,[67] W. Park,[67] M. V. Purohit,[67] J. R. Wilson,[67] M. T. Allen,[68] D. Aston,[68] R. Bartoldus,[68] P. Bechtle,[68] N. Berger,[68] R. Claus,[68] J. P. Coleman,[68] M. R. Convery,[68] J. C. Dingfelder,[68] J. Dorfan,[68] G. P. Dubois-Felsmann,[68] D. Dujmic,[68] W. Dunwoodie,[68] R. C. Field,[68] T. Glanzman,[68] S. J. Gowdy,[68] M. T. Graham,[68] P. Grenier,[68] V. Halyo,[68] C. Hast,[68] T. Hryn'ova,[68] W. R. Innes,[68] M. H. Kelsey,[68] P. Kim,[68] D. W. G. S. Leith,[68] S. Li,[68] S. Luitz,[68] V. Luth,[68] H. L. Lynch,[68] D. B. MacFarlane,[68] H. Marsiske,[68] R. Messner,[68] D. R. Muller,[68] C. P. O'Grady,[68] V. E. Ozcan,[68] A. Perazzo,[68] M. Perl,[68] T. Pulliam,[68] B. N. Ratcliff,[68] A. Roodman,[68] A. A. Salnikov,[68] R. H. Schindler,[68] J. Schwiening,[68] A. Snyder,[68] J. Stelzer,[68] D. Su,[68] M. K. Sullivan,[68] K. Suzuki,[68] S. K. Swain,[68] J. M. Thompson,[68] J. Va'vra,[68] N. van Bakel,[68] A. P. Wagner,[68] M. Weaver,[68] W. J. Wisniewski,[68] M. Wittgen,[68] D. H. Wright,[68] A. K. Yarritu,[68] K. Yi,[68] C. C. Young,[68] P. R. Burchat,[69] A. J. Edwards,[69] S. A. Majewski,[69] B. A. Petersen,[69] L. Wilden,[69] S. Ahmed,[70] M. S. Alam,[70] R. Bula,[70] J. A. Ernst,[70] V. Jain,[70] B. Pan,[70] M. A. Saeed,[70] F. R. Wappler,[70] S. B. Zain,[70] W. Bugg,[71] M. Krishnamurthy,[71] S. M. Spanier,[71] R. Eckmann,[72] J. L. Ritchie,[72] A. M. Ruland,[72] C. J. Schilling,[72] R. F. Schwitters,[72] J. M. Izen,[73] X. C. Lou,[73] S. Ye,[73] F. Bianchi,[74] F. Gallo,[74] D. Gamba,[74] M. Pelliccioni,[74] M. Bomben,[75] L. Bosisio,[75] C. Cartaro,[75] F. Cossutti,[75] G. Della Ricca,[75] L. Lanceri,[75] L. Vitale,[75] V. Azzolini,[76] N. Lopez-March,[76] F. Martinez-Vidal,[76] D. A. Milanes,[76] A. Oyanguren,[76] J. Albert,[77] Sw. Banerjee,[77] B. Bhuyan,[77] K. Hamano,[77] R. Kowalewski,[77] I. M. Nugent,[77] J. M. Roney,[77] R. J. Sobie,[77] J. J. Back,[78] P. F. Harrison,[78] T. E. Latham,[78] G. B. Mohanty,[78] M. Pappagallo,[78,§] H. R. Band,[79] X. Chen,[79] S. Dasu,[79] K. T. Flood,[79] J. J. Hollar,[79] P. E. Kutter,[79] Y. Pan,[79] M. Pierini,[79] R. Prepost,[79] S. L. Wu,[79] Z. Yu,[79] and H. Neal[80]

(*BABAR* Collaboration)

[1]*Laboratoire de Physique des Particules, IN2P3/CNRS et Université de Savoie, F-74941 Annecy-Le-Vieux, France*
[2]*Universitat de Barcelona, Facultat de Fisica, Departament ECM, E-08028 Barcelona, Spain*
[3]*Università di Bari, Dipartimento di Fisica and INFN, I-70126 Bari, Italy*
[4]*University of Bergen, Institute of Physics, N-5007 Bergen, Norway*
[5]*Lawrence Berkeley National Laboratory and University of California, Berkeley, California 94720, USA*
[6]*University of Birmingham, Birmingham, B15 2TT, United Kingdom*
[7]*Ruhr Universität Bochum, Institut für Experimentalphysik1, D-44780 Bochum, Germany*
[8]*University of Bristol, Bristol BS8 1TL, United Kingdom*
[9]*University of British Columbia, Vancouver, British Columbia, Canada V6T 1Z1*
[10]*Brunel University, Uxbridge, Middlesex UB8 3PH, United Kingdom*
[11]*Budker Institute of Nuclear Physics, Novosibirsk 630090, Russia*
[12]*University of California at Irvine, Irvine, California 92697, USA*
[13]*University of California at Los Angeles, Los Angeles, California 90024, USA*
[14]*University of California at Riverside, Riverside, California 92521, USA*
[15]*University of California at San Diego, La Jolla, California 92093, USA*
[16]*University of California at Santa Barbara, Santa Barbara, California 93106, USA*
[17]*University of California at Santa Cruz, Institute for Particle Physics, Santa Cruz, California 95064, USA*
[18]*California Institute of Technology, Pasadena, California 91125, USA*
[19]*University of Cincinnati, Cincinnati, Ohio 45221, USA*
[20]*University of Colorado, Boulder, Colorado 80309, USA*
[21]*Colorado State University, Fort Collins, Colorado 80523, USA*
[22]*Universität Dortmund, Institut für Physik, D-44221 Dortmund, Germany*
[23]*Technische Universität Dresden, Institut für Kern-und Teilchenphysik, D-01062 Dresden, Germany*
[24]*Laboratoire Leprince-Ringuet, CNRS/IN2P3, Ecole Polytechnique, F-91128 Palaiseau, France*
[25]*University of Edinburgh, Edinburgh EH9 3JZ, United Kingdom*
[26]*Università di Ferrara, Dipartimento di Fisica and INFN, I-44100 Ferrara, Italy*
[27]*Laboratori Nazionali di Frascati dell'INFN, I-00044 Frascati, Italy*

[28]*Università di Genova, Dipartimento di Fisica and INFN,I-16146 Genova, Italy*
[29]*Harvard University, Cambridge, Massachusetts 02138, USA*
[30]*Universität Heidelberg, Physikalisches Institut, Philosophenweg12, D-69120 Heidelberg, Germany*
[31]*Imperial College London, London, SW7 2AZ, United Kingdom*
[32]*University of Iowa, Iowa City, Iowa 52242, USA*
[33]*Iowa State University, Ames, Iowa 50011-3160, USA*
[34]*Johns Hopkins University, Baltimore, Maryland 21218, USA*
[35]*Universität Karlsruhe, Institut für Experimentelle Kernphysik, D-76021 Karlsruhe, Germany*
[36]*Laboratoire de l'Accélérateur Linéaire, IN2P3/CNRS et Université Paris-Sud 11, Centre Scientifique d'Orsay, B. P. 34, F-91898 ORSAY Cedex, France*
[37]*Lawrence Livermore National Laboratory, Livermore, California 94550, USA*
[38]*University of Liverpool, Liverpool L69 7ZE, United Kingdom*
[39]*Queen Mary, University of London, E1 4NS, United Kingdom*
[40]*University of London, Royal Holloway and Bedford New College,Egham, Surrey TW20 0EX, United Kingdom*
[41]*University of Louisville, Louisville, Kentucky 40292, USA*
[42]*University of Manchester, Manchester M13 9PL, United Kingdom*
[43]*University of Maryland, College Park, Maryland 20742, USA*
[44]*University of Massachusetts, Amherst, Massachusetts 01003, USA*
[45]*Massachusetts Institute of Technology, Laboratory for Nuclear Science, Cambridge, Massachusetts 02139, USA*
[46]*McGill University, Montréal, Québec, Canada H3A 2T8*
[47]*Università di Milano, Dipartimento di Fisica and INFN, I-20133 Milano, Italy*
[48]*University of Mississippi, University, Mississippi 38677, USA*
[49]*Université de Montréal, Physique des Particules, Montréal, Québec, Canada H3C 3J7*
[50]*Mount Holyoke College, South Hadley, Massachusetts 01075, USA*
[51]*Università di Napoli Federico II, Dipartimento diScienze Fisiche and INFN, I-80126, Napoli, Italy*
[52]*NIKHEF, National Institute for Nuclear Physics and High Energy Physics, NL-1009 DB Amsterdam, The Netherlands*
[53]*University of Notre Dame, Notre Dame, Indiana 46556, USA*
[54]*Ohio State University, Columbus, Ohio 43210, USA*
[55]*University of Oregon, Eugene, Oregon 97403, USA*
[56]*Università di Padova, Dipartimento di Fisica and INFN, I-35131 Padova, Italy*
[57]*Laboratoire de Physique Nucléaire et de Hautes Energies, IN2P3/CNRS, Université Pierre et Marie Curie-Paris6, Université Denis Diderot-Paris7, F-75252 Paris, France*
[58]*University of Pennsylvania, Philadelphia, Pennsylvania 19104, USA*
[59]*Università di Perugia, Dipartimento di Fisica and INFN, I-06100 Perugia, Italy*
[60]*Università di Pisa, Dipartimento di Fisica, ScuolaNormale Superiore and INFN, I-56127 Pisa, Italy*
[61]*Prairie View A&M University, Prairie View, Texas 77446, USA*
[62]*Princeton University, Princeton, New Jersey 08544, USA*
[63]*Università di Roma La Sapienza, Dipartimento di Fisica and INFN, I-00185 Roma, Italy*
[64]*Universität Rostock, D-18051 Rostock, Germany*
[65]*Rutherford Appleton Laboratory, Chilton, Didcot, Oxon, OX11 0QX, United Kingdom*
[66]*DSM/Dapnia, CEA/Saclay, F-91191 Gif-sur-Yvette, France*
[67]*University of South Carolina, Columbia, South Carolina 29208, USA*
[68]*Stanford Linear Accelerator Center, Stanford, California 94309, USA*
[69]*Stanford University, Stanford, California 94305-4060, USA*
[70]*State University of New York, Albany, New York 12222, USA*
[71]*University of Tennessee, Knoxville, Tennessee 37996, USA*
[72]*University of Texas at Austin, Austin, Texas 78712, USA*
[73]*University of Texas at Dallas, Richardson, Texas 75083, USA*
[74]*Università di Torino, Dipartimento di Fisica Sperimentale and INFN, I-10125 Torino, Italy*
[75]*Università di Trieste, Dipartimento di Fisica and INFN, I-34127 Trieste, Italy*
[76]*IFIC, Universitat de Valencia-CSIC, E-46071 Valencia, Spain*
[77]*University of Victoria, Victoria, British Columbia, Canada V8W 3P6*
[78]*Department of Physics, University of Warwick, Coventry CV47AL, United Kingdom*
[79]*University of Wisconsin, Madison, Wisconsin 53706, USA*
[80]*Yale University, New Haven, Connecticut 06511, USA*

[*]Deceased
[†]Also with Università di Perugia, Dipartimento di Fisica, Perugia, Italy
[‡]Also with Università della Basilicata, Potenza, Italy
[§]Also with IPPP, Physics Department, Durham University, Durham DH1 3LE, United Kingdom

(Received 3 March 2007; published 18 July 2007)

We report a measurement of *CP*-violating asymmetries in $B^0 \to (\rho\pi)^0 \to \pi^+\pi^-\pi^0$ decays using a time-dependent Dalitz plot analysis. The results are obtained from a data sample of 375×10^6 $\Upsilon(4S) \to B\bar{B}$ decays, collected by the *BABAR* detector at the PEP-II asymmetric-energy *B* Factory at SLAC. We measure 26 coefficients of the bilinear form-factor terms occurring in the time-dependent decay rate of the B^0 meson. We derive the physically relevant quantities from these coefficients. In particular, we measure a constraint on the angle α of the unitarity triangle.

DOI: 10.1103/PhysRevD.76.012004 PACS numbers: 13.66.Bc, 13.25.Gv, 13.25.Jx, 14.40.Cs

I. INTRODUCTION

Measurements of the parameter $\sin 2\beta$ [1,2] have established *CP* violation in the B^0 meson system. These measurements provide strong support for the Kobayashi and Maskawa model of this phenomenon as arising from a single phase in the three-generation Cabibbo-Kobayashi-Maskawa (CKM) quark-mixing matrix [3]. We present in this paper results from a time-dependent analysis of the $B^0 \to \pi^+\pi^-\pi^0$ [4] Dalitz plot which is dominated by intermediate vector resonances (ρ). The goal of this analysis is the simultaneous extraction of the strong transition amplitudes and the weak interaction phase $\alpha \equiv \arg[-V_{td}V_{tb}^*/V_{ud}V_{ub}^*]$ of the unitarity triangle. In the standard model, a nonzero value for α is responsible for the occurrence of mixing-induced *CP* violation in this decay. The *BABAR* and Belle experiments have obtained constraints on α from the measurement of effective quantities $\sin 2\alpha_{\rm eff}$ in *B* decays to $\pi^+\pi^-$ [5,6] and from $\rho^+\rho^-$ [7,8], using an isospin analysis [9].

Unlike $\pi^+\pi^-$, $\rho^\pm\pi^\mp$ is not a *CP* eigenstate and four flavor-charge configurations ($B^0(\bar{B}^0) \to \rho^\pm\pi^\mp$) must be considered. The corresponding isospin analysis [10] is unfruitful with the present data sample since two pentagonal amplitude relations with 12 unknowns have to be solved (compared to 6 unknowns for the $\pi^+\pi^-$ and $\rho^+\rho^-$ systems). However, it has been pointed out by Snyder and Quinn [11] that one can obtain the necessary degrees of freedom to constrain α without ambiguity by explicitly including in the analysis the variation of the strong phases of the interfering ρ resonances in the Dalitz plot.

A. Decay amplitudes

We consider the decay of a spin-zero B^0 meson with four-momentum p_B into the three daughters π^+, π^-, π^0, with p_+, p_-, and p_0 their corresponding four-momenta. We take as the independent (Mandelstam) variables the invariant squared masses of the charged and neutral pions

$$s_+ = (p_+ + p_0)^2, \qquad s_- = (p_- + p_0)^2. \tag{1}$$

The invariant squared mass of the positive and negative pion, $s_0 = (p_+ + p_-)^2$, is obtained, from energy and momentum conservation,

$$s_0 = m_{B^0}^2 + 2m_{\pi^+}^2 + m_{\pi^0}^2 - s_+ - s_-. \tag{2}$$

The differential B^0 decay rate distribution as a function of the variables defined in Eq. (1) (i.e., the *Dalitz plot*) reads

$$d\Gamma(B^0 \to \pi^+\pi^-\pi^0) = \frac{1}{(2\pi)^3}\frac{|A_{3\pi}|^2}{32m_{B^0}^3}ds_+ds_-, \tag{3}$$

where $A_{3\pi}$ is the Lorentz-invariant amplitude of the three-body decay [12].

We assume in the following that the amplitude $A_{3\pi}$ and its *CP* conjugate $\bar{A}_{3\pi}$, corresponding to the transitions $B^0 \to \pi^+\pi^-\pi^0$ and $\bar{B}^0 \to \pi^+\pi^-\pi^0$, respectively, are dominated by the three resonances ρ^+, ρ^-, and ρ^0. The ρ resonances are assumed to be the sum of the ground state $\rho(770)$ and the radial excitations $\rho(1450)$ and $\rho(1700)$, with masses and widths determined by a combined fit to $\tau^+ \to \bar{\nu}_\tau\pi^+\pi^0$ and $e^+e^- \to \pi^+\pi^-$ data [13]. Since the hadronic environment is different in *B* decays, we do not rely on this result for the relative $\rho(1450)$ and $\rho(1700)$ amplitudes but instead simultaneously measure them with the *CP* parameters from the fit. Variations of the other parameters and possible contributions to the $B^0 \to \pi^+\pi^-\pi^0$ decay other than the ρ resonances are studied as part of the systematic uncertainties (Sec. V).

We write the $A_{3\pi}$ and $\bar{A}_{3\pi}$ amplitudes [11,14]

$$A_{3\pi} = f_+A^+ + f_-A^- + f_0A^0, \tag{4}$$

$$\bar{A}_{3\pi} = f_+\bar{A}^+ + f_-\bar{A}^- + f_0\bar{A}^0, \tag{5}$$

where the f_κ (with $\kappa = \{+, -, 0\}$ denoting the charge of the ρ from the decay of the B^0 meson) are functions of the Dalitz variables s_+ and s_- that incorporate the kinematic and dynamical properties of the B^0 decay into a vector ρ resonance and a pseudoscalar pion. The A^κ are complex amplitudes that include weak and strong transition phases and that are independent of the Dalitz variables.

Following Ref. [13], the ρ resonances are parametrized in f_κ (where κ is the charge) as a sum of the $\rho(770)$, $\rho(1450)$, and $\rho(1700)$ resonances:

$$f_\kappa(s) \propto F_{\rho(770)}(s) + a_{\rho'}e^{i\phi_{\rho'}}F_{\rho(1450)}(s) + a_{\rho''}e^{i\phi_{\rho''}}F_{\rho(1700)}(s), \tag{6}$$

where the F_ρ are modified relativistic Breit-Wigner functions introduced by Gounaris and Sakurai (GS) [15] and the a_ρ (ϕ_ρ) are the magnitudes (phases) of the higher mass ρ resonances, relative to the $\rho(770)$. In this analysis, we

assume that the a and ϕ for f_+ and f_- are the same. For f_0, corresponding to the much smaller ρ^0 component, we fix a'_ρ and a''_ρ since the number of events expected from the excitations in the neutral band is very small. Note that the definitions (4) and (5) are based on the assumption that the relative phases between the $\rho(770)$ and its radial excitations are CP conserving.

Because of angular momentum conservation, the spin-one ρ resonance is restricted to a helicity-zero state. For a ρ^κ resonance with charge κ, the GS function is multiplied by the kinematic function $-4|\mathbf{p}_\kappa||\mathbf{p}_\tau|\cos\theta_\kappa$, where $\mathbf{p}_\kappa$ is the momentum of either of the daughters of the ρ resonance, $\mathbf{p}_\tau$ is the momentum of the particle not from the ρ decay, and $\cos\theta_\kappa$ is the cosine of the helicity angle of the ρ^κ all defined, in the ρ-resonance rest frame. For the ρ^+ (ρ^-), θ_+ (θ_-) is defined by the angle between the π^0 (π^-) momentum in the ρ^+ (ρ^-) rest frame and the ρ^+ (ρ^-) flight direction in the B^0 rest frame. For the ρ^0, θ_0 is defined by the angle between the π^+ momentum in the ρ^0 rest frame and the ρ^0 flight direction in the B^0 rest frame. With these definitions, each pair of GS functions interferes destructively at equal masses.

The factor of $\cos\theta_\kappa$ in the kinematic functions leads to an increased population in the interference regions between the different ρ bands in the Dalitz plot, and thus increases the sensitivity of this analysis [11].

B. Time dependence

With $\Delta t \equiv t_{3\pi} - t_{\rm tag}$ defined as the proper time interval between the decay of the fully reconstructed $B^0_{3\pi}$ and that of the other meson $B^0_{\rm tag}$ from the $\Upsilon(4S)$, the time-dependent decay rate $|\mathcal{A}^+_{3\pi}(\Delta t)|^2$ ($|\mathcal{A}^-_{3\pi}(\Delta t)|^2$) when the $B^0_{\rm tag}$ is a B^0 ($\bar{B}^0$) is given by

$$|\mathcal{A}^\pm_{3\pi}(\Delta t)|^2 = \frac{e^{-|\Delta t|/\tau_{B^0}}}{4\tau_{B^0}}\Big[|A_{3\pi}|^2 + |\bar{A}_{3\pi}|^2 \mp (|A_{3\pi}|^2 - |\bar{A}_{3\pi}|^2)\cos(\Delta m_d \Delta t) \pm 2\,\mathrm{Im}\Big[\frac{q}{p}\bar{A}_{3\pi}A^*_{3\pi}\Big]\sin(\Delta m_d \Delta t)\Big], \tag{7}$$

where τ_{B^0} is the mean neutral B lifetime and Δm_d is the $B^0\bar{B}^0$ mass difference. Here, we have assumed that CP violation in $B^0\bar{B}^0$ mixing is absent ($|q/p| = 1$) and the lifetime difference between B_H and B_L is $\Delta\Gamma_{B_d} = 0$. Inserting the amplitudes (4) and (5), one obtains for the terms in Eq. (7)

$$|A_{3\pi}|^2 \pm |\bar{A}_{3\pi}|^2 = \sum_{\kappa\in\{+,-,0\}} |f_\kappa|^2 U^\pm_\kappa + \sum_{\kappa<\sigma\in\{+,-,0\}} 2(\mathrm{Re}[f_\kappa f^*_\sigma]U^{\pm,\mathrm{Re}}_{\kappa\sigma} - \mathrm{Im}[f_\kappa f^*_\sigma]U^{\pm,\mathrm{Im}}_{\kappa\sigma}),$$
$$\mathrm{Im}\Big(\frac{q}{p}\bar{A}_{3\pi}A^*_{3\pi}\Big) = \sum_{\kappa\in\{+,-,0\}} |f_\kappa|^2 I_\kappa + \sum_{\kappa<\sigma\in\{+,-,0\}} (\mathrm{Re}[f_\kappa f^*_\sigma]I^{\mathrm{Im}}_{\kappa\sigma} + \mathrm{Im}[f_\kappa f^*_\sigma]I^{\mathrm{Re}}_{\kappa\sigma}), \tag{8}$$

with

$$U^\pm_\kappa = |A^\kappa|^2 \pm |\bar{A}^\kappa|^2, \tag{9}$$

$$U^{\pm,\mathrm{Re}}_{\kappa\sigma} = \mathrm{Re}[A^\kappa A^{\sigma*} \pm \bar{A}^\kappa \bar{A}^{\sigma*}], \tag{10}$$

$$U^{\pm,\mathrm{Im}}_{\kappa\sigma} = \mathrm{Im}[A^\kappa A^{\sigma*} \pm \bar{A}^\kappa \bar{A}^{\sigma*}], \tag{11}$$

$$I_\kappa = \mathrm{Im}[\bar{A}^\kappa A^{\kappa*}], \tag{12}$$

$$I^{\mathrm{Re}}_{\kappa\sigma} = \mathrm{Re}[\bar{A}^\kappa A^{\sigma*} - \bar{A}^\sigma A^{\kappa*}], \tag{13}$$

$$I^{\mathrm{Im}}_{\kappa\sigma} = \mathrm{Im}[\bar{A}^\kappa A^{\sigma*} + \bar{A}^\sigma A^{\kappa*}]. \tag{14}$$

The 27 coefficients (9)–(14) are real-valued parameters that multiply the $f_\kappa f^*_\sigma$ bilinears (where κ and σ denote the charge of the ρ resonances) [16]. These coefficients are the observables that are determined by the fit. Each of the coefficients is related in a unique way to physically more intuitive quantities, such as tree-level and penguin-type amplitudes, the angle α, or the quasi-two-body CP and dilution parameters [17] (*cf.* Sec. VI). The parametrization (8) is general: the information on the mirror solutions (e.g., on the angle α) that are present in the transition amplitudes A^κ, $\bar{A}^\kappa$ is conserved.

The decay rate (7) is used as a probability density function (PDF) in a maximum-likelihood fit and must therefore be normalized:

$$|\mathcal{A}^\pm_{3\pi}(\Delta t)|^2 \to \frac{1}{\langle |A_{3\pi}|^2 + |\bar{A}_{3\pi}|^2\rangle}|\mathcal{A}^\pm_{3\pi}(\Delta t)|^2, \tag{15}$$

where

$$\langle |A_{3\pi}|^2 + |\bar{A}_{3\pi}|^2\rangle = \sum_{\kappa\in\{+,-,0\}} \langle |f_\kappa|^2\rangle U^+_\kappa + 2\,\mathrm{Re}\sum_{\kappa<\sigma\in\{+,-,0\}} \langle f_\kappa f^*_\sigma\rangle \times (U^{+,\mathrm{Re}}_{\kappa\sigma} + i\cdot U^{+,\mathrm{Im}}_{\kappa\sigma}), \tag{16}$$

where $\langle\ldots\rangle$ denotes the expectation value over the Dalitz plot. The complex expectation values $\langle f_\kappa f^*_\sigma\rangle$ are obtained from Monte Carlo integration of the Dalitz plot (3), taking into account acceptance and resolution effects. In this paper, we determine the relative values of U and I coefficients to U^+_+ leaving 26 free coefficients.

The choice to fit for the U and I coefficients rather than fitting for the complex transition amplitudes and the weak phase α directly is motivated by the following technical simplifications: (i) in contrast to the amplitudes, there is a unique solution for the U and I coefficients requiring only a single fit to the selected data sample; (ii) in the presence of background, we find that the errors on the U and I coefficients are approximately Gaussian, which in general is not the case for the amplitudes; and (iii) the propagation of systematic uncertainties and the averaging between different measurements are straightforward for the U and I coefficients.

The U_κ^+ coefficients are related to resonance branching fractions and charge asymmetries; the U_κ^- coefficients determine the relative abundance of the B^0 decay into $\rho^+\pi^-$ and $\rho^-\pi^+$ and the time-dependent direct CP asymmetries. The I_κ measure mixing-induced CP violation and are sensitive to strong phase shifts. Finally, the $U_{\kappa\sigma}^{\pm,\mathrm{Re(Im)}}$ and $I_{\kappa\sigma}^{\mathrm{Re(Im)}}$ coefficients describe the interference pattern in the Dalitz plot, and their presence distinguishes this analysis from the quasi-two-body analysis previously reported in Ref. [17]. They represent the additional degrees of freedom that allow one to determine the unknown penguin contribution and the relative strong phases. However, because the overlap regions of the resonances are small and because the events reconstructed in these regions suffer from large misreconstruction rates and background, a substantial data sample is needed to perform a fit that constrains all amplitude parameters.

We determine the physically relevant quantities in a subsequent least-squares fit to the measured U and I coefficients.

C. The square Dalitz plot

Both the signal events and the combinatorial $e^+e^- \to q\bar{q}$ ($q = u, d, s, c$) continuum-background events populate the kinematic boundaries of the Dalitz plot due to the low final state masses compared with the B^0 mass. We find the representation (3) is inconvenient when one wants to use empirical reference shapes in a maximum-likelihood fit. Large variations occurring in small areas of the Dalitz plot are very difficult to describe in detail. These regions are particularly important since it is here that the interference between ρ resonances, and hence our ability to determine the strong phases, occurs. We therefore apply the transformation

$$ds_+ ds_- \to |\det J| dm' d\theta', \tag{17}$$

which defines the *Square Dalitz plot* (SDP). The new coordinates are

$$m' \equiv \frac{1}{\pi}\arccos\left(2\frac{m_0 - m_0^{\min}}{m_0^{\max} - m_0^{\min}} - 1\right), \qquad \theta' \equiv \frac{1}{\pi}\theta_0, \tag{18}$$

where $m_0 = \sqrt{s_0}$ is the invariant mass of the charged particles, $m_0^{\max} = m_{B^0} - m_{\pi^0}$ and $m_0^{\min} = 2m_{\pi^+}$ are the kinematic limits of m_0, θ_0 is the ρ^0 helicity angle, and J is the Jacobian of the transformation. Both new variables range between 0 and 1. The determinant of the Jacobian is given by

$$|\det J| = 4|\mathbf{p}_+^*||\mathbf{p}_0^*| m_0 \cdot \frac{\partial m_0}{\partial m'} \cdot \frac{\partial \cos\theta_0}{\partial \theta'}, \tag{19}$$

where $|\mathbf{p}_+^*| = \sqrt{E_+^{*2} - m_{\pi^+}^2}$ and $|\mathbf{p}_0^*| = \sqrt{E_0^{*2} - m_{\pi^0}^2}$, and where the energies E_+^* and E_0^* are defined in the $\pi^+\pi^-$ rest frame. Figure 1 shows the determinant of the Jacobian as a function of the SDP parameters m' and θ'. If the events in the nominal Dalitz plot were distributed according to a uniform (nonresonant) three-body phases space, their distribution in the SDP would match the plot of $|\det J|$.

The effect of the transformation (17) is illustrated in Fig. 2, which displays the nominal and square Dalitz plots for simulated signal events generated with Monte Carlo. As is shown, the transformation is beneficial because: (i) it expands the regions of interference so that equal size bins cover this region in more detail; and (ii) it avoids the curved edge of bins on the boundary. This simulation does not take into account any detector effects and corresponds to a particular choice of the decay amplitudes for which destructive interferences occur where the ρ resonances overlap. To simplify the comparison, hatched areas showing the interference regions between ρ bands and dashed isocontours $\sqrt{s_{+,-,0}} = 1.5\ \mathrm{GeV}/c^2$ have been superimposed on both Dalitz plots.

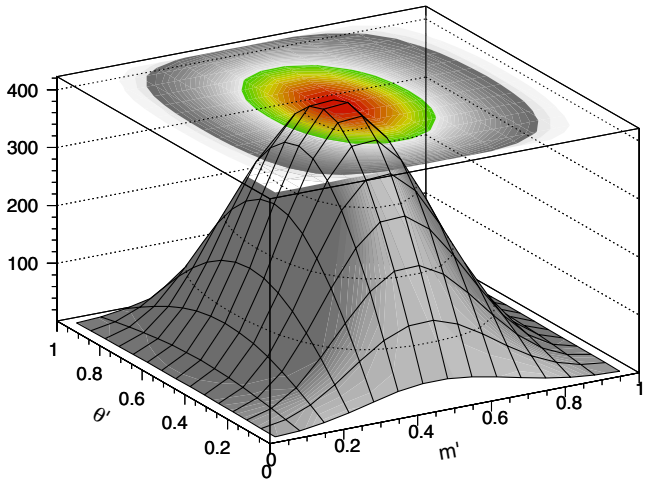

FIG. 1 (color online). Jacobian determinant (19) of the transformation (17) defining the square Dalitz plot (SDP). Such a distribution would be obtained in the SDP if events were uniformly distributed over the nominal Dalitz plot.

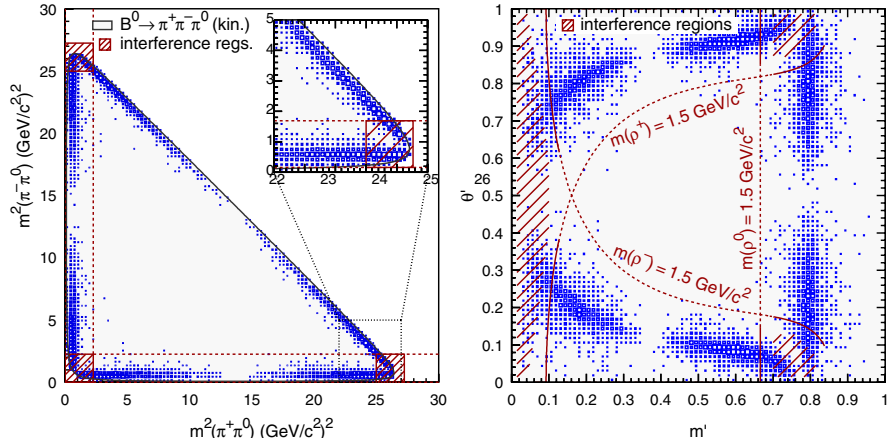

FIG. 2 (color online). Nominal (left) and square (right) Dalitz plots for Monte Carlo generated $B^0 \to \pi^+\pi^-\pi^0$ decays. Comparing the two Dalitz plots shows that the transformation (17) indeed homogenizes the distribution of events, which are no longer near the plot boundaries but rather cover a larger fraction of the physical region. The decays have been simulated without any detector effect and the amplitudes A^+, A^-, and A^0 have all been chosen equal to 1 in order to have destructive interferences where the ρ bands overlap. The main overlap regions between the ρ bands are indicated by the hatched areas. Dashed lines in both plots correspond to $\sqrt{s_{+,-,0}} = 1.5\ \mathrm{GeV}/c^2$; the central region of the Dalitz plot (defined by requiring that all 3 two-body invariant masses exceed this threshold) contains few signal events.

II. THE *BABAR* DETECTOR AND DATA SET

The data used in this analysis were collected with the *BABAR* detector at the PEP-II asymmetric-energy e^+e^- storage ring at SLAC between October 1999 and August 2006. The sample consists of about 346 fb^{-1}, corresponding to $(375 \pm 4) \times 10^6$ $B\bar{B}$ pairs collected at the $\Upsilon(4S)$ resonance ("on-resonance"), and an integrated luminosity of 21.6 fb^{-1} collected about 40 MeV below the $\Upsilon(4S)$ ("off-resonance"). In addition, we use GEANT4 [18] simulated Monte Carlo (MC) events to study detector efficiency and backgrounds.

A detailed description of the *BABAR* detector is presented in Ref. [19]. The tracking system used for charged particle and vertex reconstruction has two main components: a silicon vertex tracker (SVT) and a drift chamber (DCH), both operating within a 1.5-T magnetic field generated by a superconducting solenoid. Photons are identified in an electromagnetic calorimeter (EMC) surrounding a detector of internally reflected Cherenkov light (DIRC), which associates Cherenkov photons with tracks for particle identification (PID). Muon candidates are identified with the use of the instrumented flux return (IFR) of the solenoid.

III. ANALYSIS METHOD

The U and I coefficients and the $B^0 \to \pi^+\pi^-\pi^0$ event yield are determined by a maximum-likelihood fit of the signal and background model to the selected candidate events. Kinematic and event shape variables exploiting the characteristic properties of the events are used in the fit to discriminate signal from background.

A. Event selection and background suppression

We reconstruct $B^0 \to \pi^+\pi^-\pi^0$ candidates from pairs of oppositely charged tracks and a $\pi^0 \to \gamma\gamma$ candidate. In order to ensure that all events are within the Dalitz-plot boundary, we constrain the three-pion invariant mass to the B mass after final selections have been made. The largest source of background is from continuum $e^+e^- \to q\bar{q}$ production. We use information from the tracking system, EMC, and DIRC to remove tracks for which the PID is consistent with the electron, kaon, or proton hypotheses. In addition, we require that at least one track has a signature in the IFR that is inconsistent with the muon hypothesis. This selection retains 92% of signal events while rejecting 42% of continuum-background events. The π^0 candidate mass $m(\gamma\gamma)$ must satisfy $0.11 < m(\gamma\gamma) < 0.16\ \mathrm{GeV}/c^2$, where each photon, γ, is required to have an energy greater than 50 MeV in the laboratory frame (LAB) and to exhibit a lateral profile of energy deposition in the EMC consistent with an electromagnetic shower.

A B-meson candidate is characterized kinematically by the beam-energy substituted mass $m_{\mathrm{ES}} = \sqrt{(E^{\mathrm{cm}}_{\mathrm{beam}})^2 - (p^{\mathrm{cm}}_B)^2}$ and energy difference $\Delta E = E^*_B - \frac{1}{2}\sqrt{s}$, where $(E_B, \mathbf{p}_B)$ and $(E_0, \mathbf{p}_0)$ are the four-vectors of the B candidate and the initial electron-positron systems, respectively. The asterisk denotes the center-of-mass (CM) frame and s is the square of the CM energy. We require $5.272 < m_{\mathrm{ES}} < 5.288\ \mathrm{GeV}/c^2$, which retains 81% of the signal and 8% of the continuum-background events. The ΔE resolution exhibits a dependence on the π^0 energy and therefore varies across the Dalitz plot. To avoid bias in the Dalitz plot, we introduce the transformed quantity

$\Delta E' = (2\Delta E - \Delta E_+ - \Delta E_-)/(\Delta E_+ - \Delta E_-)$, with $\Delta E_\pm(m_0) = c_\pm - (c_\pm \mp \bar{c})(m_0/m_0^{\rm max})^2$, where $m_0 = \sqrt{s_0}$ is strongly correlated with the energy of the π^0. We use the values $\bar{c} = 0.045$ GeV, $c_- = -0.140$ GeV, $c_+ = 0.080$ GeV, $m_0^{\rm max} = 5.0$ GeV, and require $-1 < \Delta E' < 1$. These values have been obtained from Monte Carlo simulation. The requirement retains 75% (25%) of the signal (continuum) events.

Backgrounds arise primarily from random combinations of $\pi^\pm$ and π^0 candidates in continuum events. Continuum events tend to have a more "jetlike" structure than B decays which are produced nearly at rest in the CM system. To enhance discrimination between signal and continuum, we use a neural network (NN) [20] to combine four discriminating variables: the angles with respect to the beam axis of the B momentum and B thrust axis in the $\Upsilon(4S)$ frame, and the zeroth and second-order polynomials $L_{0,2}$ of the energy flow about the B thrust axis. The polynomials are defined by $L_n = \sum_i p_i \cdot |\cos\theta_i|^n$, where θ_i is the angle with respect to the B thrust axis of any track or neutral cluster i, $\mathbf{p}_i$ is its momentum, and the sum excludes the B candidate. The NN is trained with off-peak data and simulated signal events. The final sample of signal candidates is selected with a requirement on the NN output that retains 77% (8%) of the signal (continuum) events. A total of 35 444 on-peak data events pass the selection.

The time difference Δt is obtained from the measured distance between the z positions (along the beam direction) of the $B^0_{3\pi}$ and $B^0_{\rm tag}$ decay vertices, and the boost $\beta\gamma = 0.56$ of the e^+e^- system: $\Delta t = \Delta z/\beta\gamma c$. The $B^0_{\rm tag}$ vertex is determined from the charged particles in the event not included in the signal B. To determine the flavor of the $B^0_{\rm tag}$ we use the B flavor-tagging algorithm of Ref. [1]. This produces six mutually exclusive tagging categories. We improve the efficiency of the signal selection by retaining untagged events in a seventh category which contribute to the measurement of direct CP violation.

Multiple B candidates passing the full selection occur in 16% ($\rho^\pm\pi^\mp$) and 9% ($\rho^0\pi^0$) of $\rho(770)$ MC events. If the multiple candidates have different π^0 candidates, we choose the B candidate with the reconstructed π^0 mass closest to the nominal π^0 mass; in the case that more than one candidate have the same π^0, we arbitrarily chose a reconstructed B candidate passing the selection (this occurs in 4% of events).

The signal efficiency determined from MC simulation is 24% for $B^0 \to \rho^\pm\pi^\mp$ and $B^0 \to \rho^0\pi^0$ events, and 11% for nonresonant $B^0 \to \pi^+\pi^-\pi^0$ events. The signal efficiency distribution on the SDP is shown in Fig. 3.

The signal events passing the event selection are a combination of correctly reconstructed ("truth-matched," TM) events and misreconstructed ("self-cross-feed," SCF) events. Of the selected signal events, 22% of $B^0 \to \rho^\pm\pi^\mp$, 13% of $B^0 \to \rho^0\pi^0$, and 6% of nonresonant events are misreconstructed, according to MC. Misreconstructed

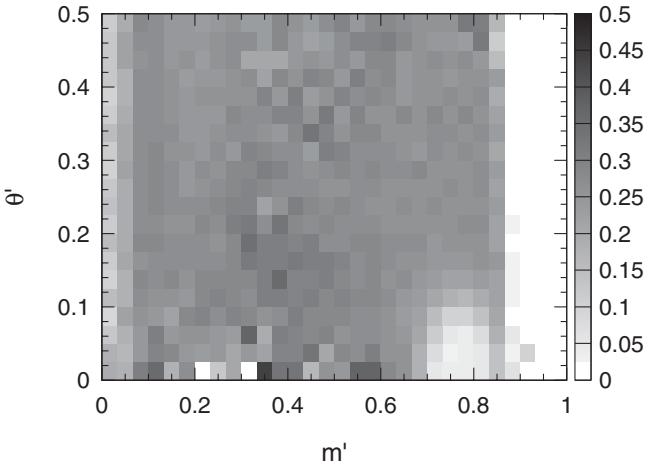

FIG. 3. The signal efficiency distribution on the square Dalitz plot. Note that the plot is folded in θ' since the distribution is nearly symmetric in this variable.

events occur when a track or neutral cluster from the tagging B is assigned to the reconstructed signal candidate. This occurs most often for low-momentum particles and photons; hence the misreconstructed events are concentrated in the corners of the standard Dalitz plot. Since these are also the areas where the ρ resonances overlap strongly, it is important to model the misreconstructed events correctly. The details of the model for the distributions of misreconstructed events in the Dalitz plot are described in Sec. III C 1.

B. Background from other B decays

We use MC simulated events to study the background from other B decays. More than one hundred channels were considered in these studies, of which 29 are included in the final likelihood model. These exclusive B-background modes are grouped into 18 different classes according to their kinematic and topological properties: six for charmless B^+ decays, eight for charmless B^0 decays, and four for exclusive charmed B^0 decays. Two additional classes account for inclusive B^0 and B^+ charmed decays.

Table I summarizes the 20 background classes that are used in the fit. For each mode, the expected number of selected events is computed by multiplying the selection efficiency (estimated using MC simulated decays) by the branching fraction, scaled to the data set luminosity (346 fb^{-1}). The world average branching ratios have been used for the experimentally known decay modes [12,21]. When only upper limits are given, they have been translated into branching ratios including additional conservative hypotheses (e.g., 100% longitudinal polarization for $B \to \rho\rho$ decay) if needed.

C. The maximum-likelihood fit

We perform an unbinned extended maximum-likelihood fit to extract the total $B^0 \to \pi^+\pi^-\pi^0$ event yield, and the

TABLE I. Summary of the B-background modes taken into account for the likelihood model. They have been grouped in 20 classes: charmless B^+ (six), charmless B^0 (eight), exclusive charmed B^0 (four), and inclusive B^0 and charmed B^+ decays. Modes with at least two events expected after final selection have been included.

Class	Mode	BR $[10^{-6}]$	Expected number of events
1	$B^+ \to \rho^+ \rho^0_{[\mathrm{long}]}$	19.1 ± 3.5	57 ± 11
1	$B^+ \to a_1^+(\to (\rho\pi)^+)\pi^0$	20.0 ± 15.0	35 ± 26
1	$B^+ \to a_1^0(\to \rho^\pm \pi^\mp)\pi^+$	20.0 ± 15.0	21 ± 15
2	$B^+ \to \pi^+ \rho^0$	8.7 ± 1.0	81 ± 9
3	$B^+ \to \rho^0 K^+$	4.3 ± 0.6	7 ± 1
3	$B^+ \to \pi^+ K^0_S(\to \pi^+\pi^-)$	8.3 ± 0.4	11 ± 1
4	$B^+ \to \pi^0 \rho^+$	10.8 ± 1.4	70 ± 9
4	$B^+ \to \pi^+ K^0_S(\to \pi^0\pi^0)$	3.7 ± 0.2	17 ± 2
5	$B^+ \to \pi^+ \pi^0$	5.5 ± 0.6	15 ± 2
5	$B^+ \to K^+ \pi^0$	12.1 ± 0.8	9 ± 1
6	$B^+ \to (K^{(**)}(1430)\pi)^+ \to (K^+\pi\pi)^+$	29.0 ± 5.4	42 ± 6
7	$B^0 \to \pi^- K^{\star+}(\to K^0_S \pi^+)$	3.3 ± 0.4	2 ± 1
8	$B^0 \to \rho^+ \rho^-_{[\mathrm{long}]}$	25.2 ± 3.7	74 ± 11
8	$B^0 \to (a_1\pi)^0$	39.7 ± 3.7	43 ± 4
9	$B^0 \to K^+ \pi^-$	18.9 ± 0.7	13 ± 1
10	$B^0 \to \pi^- K^{\star+}(\to K^+\pi^0)$	3.3 ± 0.4	22 ± 2
10	$B^0 \to K^{(**)}(1430)\pi \to K\pi\pi^0$	11.2 ± 2.2	234 ± 37
11	$B^0 \to \gamma K^{\star 0}(892\,1430)(\to (K^+\pi^-)^0)$	27.4 ± 1.5	15 ± 1
11	$B^0 \to \pi^0 K^{\star 0}(\to K^+\pi^-)$	1.3 ± 0.5	10 ± 4
11	$B^0 \to \eta'(\to \rho^0\gamma)\pi^0$	0.4 ± 0.2	3 ± 2
12	$B^0 \to \rho^- K^+$	9.9 ± 1.6	114 ± 17
13	$B^0 \to K^+\pi^-\pi^0_{[\mathrm{nonres}]}$	4.6 ± 4.6	42 ± 38
14	$B^0 \to \pi^0 K^0_S(\to \pi^+\pi^-)$	5.8 ± 0.5	55 ± 4
15	$B^0 \to D^-(\to \pi^-\pi^0)\pi^+$	7.5 ± 2.3	661 ± 203
16	$B^0 \to \bar{D}^0(\to K^+\pi^-)\pi^0$	11.0 ± 3.2	110 ± 32
17	$B^0 \to \bar{D}^0(\to \pi^+\pi^-)\pi^0$	0.4 ± 0.1	39 ± 10
18	$B^0 \to J/\psi(\to e^+e^-, \mu^+\mu^-)\pi^0$	2.6 ± 0.5	85 ± 17
19	$B^0 \to \{\text{neutral generic } b \to c \text{ decays}\}$	—	188 ± 30
20	$B^+ \to \{\text{charged generic } b \to c \text{ decays}\}$	—	431 ± 40

U and I coefficients defined in Eqs. (9)–(14). The fit uses the variables Δt, m', θ', m_{ES}, $\Delta E'$, and NN output to discriminate signal from background. The Δt distribution is sensitive to mixing-induced CP violation but also provides additional continuum-background rejection.

The selected on-resonance data sample is assumed to consist of signal, continuum-background, and B-background components, separated by the flavor and tagging category of the tag side B decay. The probability density function $\mathcal{P}_i^c$ for event i in tagging category c is the sum of the probability densities of all components, namely

$$\mathcal{P}_i^c \equiv N_{3\pi} f^c_{3\pi}[(1-\bar{f}^c_{\mathrm{SCF}})\mathcal{P}^c_{3\pi-\mathrm{TM},i} + \bar{f}^c_{\mathrm{SCF}}\mathcal{P}^c_{3\pi-\mathrm{SCF},i}] + N^c_{q\bar{q}}\frac{1}{2}(1 + q_{\mathrm{tag},i}A_{q\bar{q},\mathrm{tag}})\mathcal{P}^c_{q\bar{q},i} + \sum_{j=1}^{N^{B^+}_{\mathrm{class}}} N_{B^+j} f^c_{B^+j}\frac{1}{2}(1 + q_{\mathrm{tag},i}A_{B^+,\mathrm{tag},j})\mathcal{P}^c_{B^+,ij} + \sum_{j=1}^{N^{B^0}_{\mathrm{class}}} N_{B^0j} f^c_{B^0j}\mathcal{P}^c_{B^0,ij}, \quad (20)$$

where $N_{3\pi}$ is the total number of $\pi^+\pi^-\pi^0$ signal events in the data sample; $f^c_{3\pi}$ is the fraction of signal events that are in tagging category c; $\bar{f}^c_{\mathrm{SCF}}$ is the fraction of SCF events in tagging category c, averaged over the Dalitz plot; $\mathcal{P}^c_{3\pi-\mathrm{TM},i}$ and $\mathcal{P}^c_{3\pi-\mathrm{SCF},i}$ are the products of PDFs of the discriminating variables used in tagging category c for TM and SCF events, respectively; $N^c_{q\bar{q}}$ is the number of continuum events that are in tagging category c; $q_{\mathrm{tag},i}$ is the tag flavor

of the event, defined to be $+1$ for a $B^0_{\rm tag}$ and -1 for a $\bar{B}^0_{\rm tag}$; $A_{q\bar{q},{\rm tag}}$ parametrizes possible flavor tag asymmetry in continuum events (this is allowed to float in the fit and is found to be 0.03 ± 0.01); $\mathcal{P}^c_{q\bar{q},i}$ is the continuum PDF for tagging category c; $N^{B^+}_{\rm class}$ ($N^{B^0}_{\rm class}$) is the number of charged (neutral) B-related background classes considered in the fit; N_{B^+j} (N_{B^0j}) is the number of expected events in the charged (neutral) B-background class j; $f^c_{B^+j}$ ($f^c_{B^0j}$) is the fraction of charged (neutral) B-background events of class j that are in tagging category c; $A_{B^+,{\rm tag},j}$ describes a possible flavor tag asymmetry in the B^+ background class j; $\mathcal{P}^c_{B^+,ij}$ is the B^+-background PDF for tagging category c and class j; and $\mathcal{P}^c_{B^0,ij}$ is the neutral-B-background PDF for tagging category c and class j. Correlations between the flavor tag and the position in the Dalitz plot are absorbed in tag-flavor-dependent Dalitz-plot PDFs that are used for B^+ and continuum background.

The PDFs $\mathcal{P}^c_X$ ($X = \{{\rm TM}, {\rm SCF}, q\bar{q}, B^+/B^0\}$) are the product of the four PDFs of the discriminating variables, $x_1 = m_{\rm ES}$, $x_2 = \Delta E'$, and $x_3 = {\rm NN\ output}$, and the quadruplet $x_4 = \{m', \theta', \Delta t, q_{\rm tag}\}$:

$$\mathcal{P}^{\,c}_{X,i(j)} \equiv \prod_{k=1}^{4} P^c_{X,i(j)}(x_k), \tag{21}$$

where i is the event index and j is a B-background class. The extended likelihood over all tagging categories is given by

$$\mathcal{L} \equiv \prod_{c=1}^{7} e^{-\bar{N}^c} \prod_{i=1}^{N^c} \mathcal{P}^c_i, \tag{22}$$

where $\bar{N}^c$ is the total number of events expected in category c.

A total of 68 parameters, including the inclusive signal yield $N_{3\pi}$ and the 26 U and I coefficients from Eq. (7), are varied in the fit. Most of the parameters describing the continuum distributions are also free in the fit. The parametrizations of the PDFs are described below and are summarized in Table II.

TABLE II. Summary of PDF parametrizations where G = Gaussian, PX = X-order polynomial, NP = nonparametric, and biCB = bifurcated crystal ball. See Sec. III C 1 for a detailed description of the Dalitz-plot parametrization for signal.

Variable	TM signal	SCF signal	Continuum	B background
ΔE	GG	G	P2	NP
$m_{\rm ES}$	biCB	NP	Argus	NP
Neural net	NP	NP	P3	NP
Dalitz	see text	see text	NP	NP
Δt	GGG	GGG	GGG	GGG

1. The Δt and Dalitz-plot PDFs

The Dalitz-plot PDFs require as input the Dalitz-plot-dependent relative selection efficiency $\varepsilon = \varepsilon(m', \theta')$, and the SCF fraction, $f_{\rm SCF} = f_{\rm SCF}(m', \theta')$. Both quantities are taken from MC simulation. Away from the Dalitz-plot corners the efficiency is uniform, while it decreases when approaching the corners where one of the three particles in the final state is almost at rest in the LAB frame so that the acceptance requirements on the particle reconstruction become restrictive. Combinatorial backgrounds, and hence SCF fractions, are large in the corners of the Dalitz plot due to the presence of soft neutral clusters and tracks.

For an event i, we define the time-dependent Dalitz-plot PDFs

$$P^c_{3\pi-{\rm TM},i} \equiv \varepsilon_i(1 - f^c_{{\rm SCF},i})|\det J_i||\mathcal{A}^{\pm}_{3\pi}(\Delta t)|^2, \tag{23}$$

$$P^c_{3\pi-{\rm SCF},i} \equiv \varepsilon_i f^c_{{\rm SCF},i}|\det J_i||\mathcal{A}^{\pm}_{3\pi}(\Delta t)|^2, \tag{24}$$

where $P_{3\pi-{\rm TM},i}$ and $P_{3\pi-{\rm SCF},i}$ are normalized. The normalization involves the expectation values $\langle\varepsilon(1 - f_{\rm SCF})|\det J|f^\kappa f^{\sigma *}\rangle$ and $\langle\varepsilon f_{\rm SCF}|\det J|f^\kappa f^{\sigma *}\rangle$ for TM and SCF events, where the indices κ, σ run over all resonances belonging to the signal model. The expectation values are model dependent and are computed with the use of MC integration over the square Dalitz plot:

$$\langle\varepsilon(1 - f_{\rm SCF})|\det J|f^\kappa f^{\sigma *}\rangle = \frac{\int_0^1\int_0^1 \varepsilon(1 - f_{\rm SCF})|\det J|f^\kappa f^{\sigma *}dm'd\theta'}{\int_0^1\int_0^1 \varepsilon|\det J|f^\kappa f^{\sigma *}dm'd\theta'}, \tag{25}$$

and similarly for $\langle f_{\rm SCF}\varepsilon|\det J|f^\kappa f^{\sigma *}\rangle$, where all quantities in the integrands are Dalitz-plot dependent.

Equation (20) invokes the phase space-averaged SCF fraction $\bar{f}_{\rm SCF} \equiv \langle f_{\rm SCF}|\det J|f^\kappa f^{\sigma *}\rangle$. The PDF normalization is decay-dynamics dependent and is computed iteratively. We determine the average SCF fractions separately for each tagging category from MC simulation.

The width of the dominant $\rho(770)$ resonance is large compared to the mass resolution for TM events (about 8 MeV/c^2 Gaussian resolution). We therefore neglect resolution effects in the TM model. Misreconstructed events have a poor mass resolution that strongly varies across the Dalitz plot. These events are described in the fit by a two-dimensional resolution function

$$R_{\rm SCF}(m'_r, \theta'_r, m'_t, \theta'_t), \tag{26}$$

which represents the probability to reconstruct at the coordinate (m'_r, θ'_r) an event that has the true coordinate (m'_t, θ'_t). This function obeys the unitary condition

$$\int_0^1\int_0^1 R_{\rm SCF}(m'_r, \theta'_r, m'_t, \theta'_t)dm'_r d\theta'_r = 1, \tag{27}$$

and is convolved with the signal model. The $R_{\rm SCF}$ function is obtained from MC simulation.

The dynamical information in the signal model is described in Sec. I A and is connected with Δt via the matrix element in Eq. (7), which serves as the PDF. The PDF is modified by the effects of mistagging and the limited vertex resolution [17]. The Δt resolution function for signal and B-background events is a sum of three Gaussian distributions, with parameters determined by a fit to fully reconstructed B^0 decays [1]. Since the majority of SCF events arise from misreconsructed π^0 decays which do not affect the vertex resolution, we use the same resolution function for TM and SCF events.

The Dalitz-plot and Δt-dependent PDFs factorize for the charged-B background modes, but not necessarily for the B^0 background due to $B^0\bar{B}^0$ mixing.

The charged B-background contribution to the likelihood (20) involves the parameter $A_{B^+,\mathrm{tag}}$, multiplied by the tag flavor q_{tag} of the event. In the presence of significant ''tag-charge'' correlation (represented by an effective flavor tag versus Dalitz coordinate correlation), it parametrizes possible fake direct CP violation or asymmetries due to detector effects in these events. We also use separate square Dalitz-plot PDFs for B^0 and $\bar{B}^0$ flavor tags, and a flavor-tag-averaged PDF for untagged events. The PDFs are obtained from MC simulation and are described with the use of nonparametric functions. The Δt resolution parameters are determined by a fit to fully reconstructed B^+ decays. For each B^+-background class we obtain effective lifetimes from MC to account for the misreconstruction of the event that modifies the nominal Δt resolution function.

The neutral-B background is parametrized with PDFs that depend on the flavor tag of the event. In the case of CP eigenstates, correlations between the flavor tag and the Dalitz coordinate are expected to be small. However, non-CP eigenstates, such as $a_1^{\pm}\pi^{\mp}$, may exhibit such correlations. Both types of decays can have direct and mixing-induced CP violation. A third type of decay involves charged kaons (e.g. $\rho^{\pm}K^{\mp}$) and does not exhibit mixing-induced CP violation, but usually has a strong correlation between the flavor tag and the Dalitz-plot coordinate, because these decays correspond to B-flavor eigenstates. The Dalitz-plot PDFs are obtained from MC simulation and are described with the use of nonparametric functions. For neutral-B background, the signal Δt resolution model is assumed.

The Dalitz-plot treatment of the continuum events is similar to that used for charged-B background. The square Dalitz-plot PDF for continuum background is obtained from on-resonance events selected in the m_{ES} sidebands (defined as $5.225 < m_{\mathrm{ES}} < 5.265$) and corrected for a 5% feed-through from B decays. A large number of cross checks have been performed to ensure the high fidelity of the empirical shape parametrization. Dalitz plot-dependent flavor tag asymmetry is observed in continuum. We find that the dependence can be described by a single asymmetry parameter dependent linearly on m'. The continuum Δt distribution is parametrized as the sum of three Gaussian distributions with common mean and three distinct widths. The widths scale with the estimated Δt uncertainty for each event. This yields six shape parameters that are determined by the fit. The model is motivated by the observation that the Δt average is independent of its error, and that the Δt RMS depends linearly on the Δt error.

2. Parametrization of the other variables

The m_{ES} distribution of TM signal events is parametrized by a bifurcated crystal ball function [22], which is a combination of a one-sided Gaussian and a crystal ball function, given as:

$$f(x) = \begin{cases} Ce^{(x-m)^2/2s_R^2} & \text{for } (x-m) > 0, \\ Ce^{(x-m)^2/2s_L^2} & \text{for } 0 > \frac{x-m}{s_L} > -A, \\ C\left(\frac{b}{A}\right)^b e^{-(A^2/2)}\left(\frac{b}{A} - A - \frac{x-m}{s_L}\right)^{-b} & \text{for } \frac{x-m}{s_L} < -A. \end{cases} \tag{28}$$

The peak position of this function, m, is determined by the fit to on-peak data while the other parameters are taken from signal MC. A nonparametric function [23] is used to describe the SCF signal component.

The $\Delta E'$ distribution of TM events is parametrized by a double Gaussian function, where all five parameters depend linearly on m_0^2. The parameters of the narrow Gaussian are determined by the fit to data while the others are obtained from signal MC. Misreconstructed events are parametrized by a broad single Gaussian function whose parameters are taken from signal MC.

Both m_{ES} and $\Delta E'$ PDFs are parametrized by nonparametric functions for all B-background classes. Continuum events are parametrized with an Argus shape function [24]

$$f(m_{\mathrm{ES}}) = C\frac{m_{\mathrm{ES}}}{m_{\mathrm{ES}}^{\max}}\sqrt{1-\left(\frac{m_{\mathrm{ES}}}{m_{\mathrm{ES}}^{\max}}\right)^2}\, e^{-\xi(1-(m_{\mathrm{ES}}/m_{\mathrm{ES}}^{\max})^2)} \tag{29}$$

and a second-order polynomial in $\Delta E'$, with parameters determined by the fit. The value of $m_{\mathrm{ES}}^{\max}$ is 5.2886 GeV/c^2.

We use nonparametric functions to empirically describe the distributions of the NN outputs found in the MC simulation for TM and SCF signal events, and for B-background events. We distinguish tagging categories for TM signal events to account for differences observed in the shapes.

The continuum NN distribution is parametrized by a third-order polynomial. The coefficients of the polynomial are determined by the fit. Continuum events exhibit a correlation between the Dalitz-plot coordinate and the inputs to the NN. To account for this correlation, we introduce a linear dependence of the polynomial coefficients on the distance of the Dalitz-plot coordinate from kinematic boundaries of the Dalitz plot. The parameters describing this dependence are determined by the fit.

IV. FIT RESULTS

The maximum-likelihood fit results in a $B^0 \to \pi^+\pi^-\pi^0$ event yield of $N_{3\pi} = 2067 \pm 86$, where the error is statistical only. The results for the U and I coefficients are given together with their statistical and systematic errors in Table III. The corresponding correlation matrix is given in Table IV. We have generated a sample of Monte Carlo experiments to determine the probability density distributions of the fit parameters. Within the statistical uncertainties of this sample we find Gaussian distributions for the fitted U and I coefficients. This allows us to use the least-squares method to derive other quantities from these (Sec. VI).

The signal is dominated by $B^0 \to \rho^\pm\pi^\mp$ decays. We observe an excess of $\rho^0\pi^0$ events (see, mainly, $\mathcal{U}_0^+$), which is in agreement with our previous upper limit [25] and the latest measurement from the Belle collaboration [26]. We find the ratio of $\rho(1450)/\rho(770)$ ($\rho(1700)/\rho(770)$) rates to be 0.13 ± 0.04 (0.07 ± 0.04) where the errors are statistical only. For the relative strong phase between the $\rho(770)$ and $\rho(1450)$ ($\rho(1700)$) amplitudes we find $(163 \pm 22)^\circ$ ($(5 \pm 36)^\circ$ (statistical errors only), which is compatible with the result from τ and e^+e^- data. These results for the ρ amplitudes are compatible with the findings in τ and e^+e^- decays [13].

Figure 4 shows distributions of $\Delta E'$, $m_{\rm ES}$, the NN output, and $\Delta t/\sigma(\Delta t)$, where $\sigma(\Delta t)$ is the per-event error on Δt, as well as the Dalitz-plot variables m' and θ'. All distributions are enhanced in signal content by selecting on the ratio of the probability the event is signal to the total, $P_sig/\sum P$, excluding the variable plotted. Figure 5 shows the distribution of the minimum of the three di-pion invariant masses, again enhanced in signal content. This plot shows

TABLE III. Fit results for the U and I coefficients. The errors given are statistical (first) and systematic (second). The free normalization parameter U_+^+ is fixed to 1. The coefficients are defined in Eq. (8).

Parameter	Description	Result
U_+^+	Coefficient of $\lvert f_+\rvert^2$	1.0 (fixed)
U_0^+	Coefficient of $\lvert f_0\rvert^2$	$0.28 \pm 0.07 \pm 0.04$
U_-^+	Coefficient of $\lvert f_-\rvert^2$	$1.32 \pm 0.12 \pm 0.05$
U_0^-	Coefficient of $\lvert f_0\rvert^2 \cos(\Delta m_d \Delta t)$	$-0.03 \pm 0.11 \pm 0.09$
U_-^-	Coefficient of $\lvert f_-\rvert^2 \cos(\Delta m_d \Delta t)$	$-0.32 \pm 0.14 \pm 0.05$
U_+^-	Coefficient of $\lvert f_+\rvert^2 \cos(\Delta m_d \Delta t)$	$0.54 \pm 0.15 \pm 0.05$
I_0	Coefficient of $\lvert f_0\rvert^2 \sin(\Delta m_d \Delta t)$	$0.01 \pm 0.06 \pm 0.01$
I_-	Coefficient of $\lvert f_-\rvert^2 \sin(\Delta m_d \Delta t)$	$-0.01 \pm 0.10 \pm 0.02$
I_+	Coefficient of $\lvert f_+\rvert^2 \sin(\Delta m_d \Delta t)$	$-0.02 \pm 0.10 \pm 0.03$
$U_{+-}^{+,\rm Im}$	Coefficient of $\mathrm{Im}[f_+ f_-^*]$	$-0.07 \pm 0.71 \pm 0.73$
$U_{+-}^{+,\rm Re}$	Coefficient of $\mathrm{Re}[f_+ f_-^*]$	$0.17 \pm 0.49 \pm 0.31$
$U_{+-}^{-,\rm Im}$	Coefficient of $\mathrm{Im}[f_+ f_-^*]\cos(\Delta m_d \Delta t)$	$-0.38 \pm 1.06 \pm 0.36$
$U_{+-}^{-,\rm Re}$	Coefficient of $\mathrm{Im}[f_+ f_-^*]\cos(\Delta m_d \Delta t)$	$2.23 \pm 1.00 \pm 0.43$
$I_{+-}^{\rm Im}$	Coefficient of $\mathrm{Re}[f_+ f_-^*]\sin(\Delta m_d \Delta t)$	$-1.99 \pm 1.25 \pm 0.34$
$I_{+-}^{\rm Re}$	Coefficient of $\mathrm{Im}[f_+ f_-^*]\sin(\Delta m_d \Delta t)$	$1.90 \pm 2.03 \pm 0.65$
$U_{+0}^{+,\rm Im}$	Coefficient of $\mathrm{Im}[f_+ f_0^*]$	$-0.16 \pm 0.57 \pm 0.14$
$U_{+0}^{+,\rm Re}$	Coefficient of $\mathrm{Re}[f_+ f_0^*]$	$-1.08 \pm 0.48 \pm 0.20$
$U_{+0}^{-,\rm Im}$	Coefficient of $\mathrm{Im}[f_+ f_0^*]\cos(\Delta m_d \Delta t)$	$-1.66 \pm 0.94 \pm 0.25$
$U_{+0}^{-,\rm Re}$	Coefficient of $\mathrm{Re}[f_+ f_0^*]\cos(\Delta m_d \Delta t)$	$-0.18 \pm 0.88 \pm 0.35$
$I_{+0}^{\rm Im}$	Coefficient of $\mathrm{Re}[f_+ f_0^*]\sin(\Delta m_d \Delta t)$	$-0.21 \pm 1.06 \pm 0.25$
$I_{+0}^{\rm Re}$	Coefficient of $\mathrm{Im}[f_+ f_0^*]\sin(\Delta m_d \Delta t)$	$0.41 \pm 1.30 \pm 0.41$
$U_{-0}^{+,\rm Im}$	Coefficient of $\mathrm{Im}[f_- f_0^*]$	$-0.17 \pm 0.50 \pm 0.23$
$U_{-0}^{+,\rm Re}$	Coefficient of $\mathrm{Re}[f_- f_0^*]$	$-0.36 \pm 0.38 \pm 0.08$
$U_{-0}^{-,\rm Im}$	Coefficient of $\mathrm{Im}[f_- f_0^*]\cos(\Delta m_d \Delta t)$	$0.12 \pm 0.75 \pm 0.22$
$U_{-0}^{-,\rm Re}$	Coefficient of $\mathrm{Re}[f_- f_0^*]\cos(\Delta m_d \Delta t)$	$-0.63 \pm 0.72 \pm 0.32$
$I_{-0}^{\rm Im}$	Coefficient of $\mathrm{Re}[f_- f_0^*]\sin(\Delta m_d \Delta t)$	$1.23 \pm 1.07 \pm 0.29$
$I_{-0}^{\rm Re}$	Coefficient of $\mathrm{Im}[f_- f_0^*]\sin(\Delta m_d \Delta t)$	$0.41 \pm 1.30 \pm 0.21$

TABLE IV. Correlation matrix of statistical uncertainties for the U and I coefficients. Since the matrix is symmetric, all elements above the diagonal are omitted.

	$N_{3\pi}$	I_0	I_-	I_{-0}^{Im}	I_{-0}^{Re}	I_+	I_{+0}^{Im}	I_{+0}^{Re}	I_{+-}^{Im}	I_{+-}^{Re}	U_0^-	U_0^+	$U_{-0}^{-,\mathrm{Im}}$
$N_{3\pi}$	1.00												
I_0	−0.02	1.00											
I_-	−0.04	−0.04	1.00										
I_{-0}^{Im}	−0.09	−0.11	0.28	1.00									
I_{-0}^{Re}	−0.03	0.28	−0.18	−0.15	1.00								
I_+	0.06	−0.04	−0.20	−0.21	0.17	1.00							
I_{+0}^{Im}	0.06	−0.03	−0.11	−0.14	0.09	0.38	1.00						
I_{+0}^{Re}	−0.17	0.30	0.18	0.17	−0.06	−0.35	−0.45	1.00					
I_{+-}^{Im}	0.09	0.11	0.14	−0.17	0.10	0.21	0.11	−0.03	1.00				
I_{+-}^{Re}	−0.24	0.04	0.36	0.28	−0.15	−0.46	−0.25	0.43	−0.01	1.00			
U_0^-	−0.03	0.07	0.08	−0.05	−0.11	−0.06	−0.02	0.13	0.09	0.15	1.00		
U_0^+	0.04	−0.02	0.20	0.32	−0.19	−0.24	−0.19	0.30	−0.13	0.35	0.11	1.00	
$U_{-0}^{-,\mathrm{Im}}$	0.01	0.13	−0.11	−0.14	0.42	0.14	0.08	−0.07	0.10	−0.13	−0.36	−0.18	1.00
$U_{-0}^{-,\mathrm{Re}}$	0.02	0.07	−0.05	−0.44	0.03	0.06	0.05	0.01	0.17	−0.06	0.04	−0.19	0.13
$U_{-0}^{+,\mathrm{Im}}$	0.07	0.18	−0.14	−0.39	0.21	0.22	0.18	−0.14	0.27	−0.26	0.03	−0.56	0.31
$U_{-0}^{+,\mathrm{Re}}$	−0.05	0.16	0.07	−0.21	0.07	−0.01	−0.01	0.14	0.25	0.08	0.09	−0.05	0.19
U_-^-	0.11	−0.01	−0.03	−0.06	0.01	0.01	0.02	−0.06	0.01	−0.08	−0.09	−0.08	0.12
U_-^+	−0.12	0.14	0.08	−0.02	0.08	−0.06	−0.06	0.22	0.06	0.20	0.11	0.18	0.10
$U_{+0}^{-,\mathrm{Im}}$	0.26	0.03	−0.17	−0.19	0.10	0.17	0.11	−0.20	0.08	−0.40	−0.26	−0.31	0.15
$U_{+0}^{-,\mathrm{Re}}$	0.13	−0.02	0.00	0.08	−0.18	−0.13	−0.23	0.07	−0.05	−0.05	−0.04	0.03	−0.11
$U_{+0}^{+,\mathrm{Im}}$	0.03	0.12	−0.17	−0.41	0.36	0.34	0.34	−0.31	0.25	−0.29	−0.02	−0.54	0.29
$U_{+0}^{+,\mathrm{Re}}$	0.23	−0.03	−0.16	−0.25	0.13	0.25	0.28	−0.49	0.16	−0.44	−0.12	−0.36	0.12
$U_{+-}^{-,\mathrm{Im}}$	−0.14	−0.04	0.03	0.15	−0.04	−0.08	−0.07	0.09	−0.11	0.19	0.01	0.13	−0.08
$U_{+-}^{-,\mathrm{Re}}$	−0.12	−0.10	−0.05	0.14	−0.05	−0.01	−0.04	−0.01	−0.20	0.07	−0.10	0.09	−0.04
$U_{+-}^{+,\mathrm{Im}}$	0.12	−0.20	−0.09	0.18	−0.21	−0.03	−0.01	−0.17	−0.18	−0.22	−0.17	0.02	−0.17
$U_{+-}^{+,\mathrm{Re}}$	−0.15	0.05	0.07	0.01	0.06	0.00	−0.03	0.12	0.22	0.13	0.10	0.10	0.03
U_+^-	−0.05	−0.01	0.00	0.05	−0.06	−0.07	−0.05	0.05	−0.03	0.04	−0.03	0.05	−0.04

	$U_{-0}^{-,\mathrm{Re}}$	$U_{-0}^{+,\mathrm{Im}}$	$U_{-0}^{+,\mathrm{Re}}$	U_-^-	U_-^+	$U_{+0}^{-,\mathrm{Im}}$	$U_{+0}^{-,\mathrm{Re}}$	$U_{+0}^{+,\mathrm{Im}}$	$U_{+0}^{+,\mathrm{Re}}$	$U_{+-}^{-,\mathrm{Im}}$	$U_{+-}^{-,\mathrm{Re}}$	$U_{+-}^{+,\mathrm{Im}}$	$U_{+-}^{+,\mathrm{Re}}$	U_+^-
$U_{-0}^{-,\mathrm{Re}}$	1.00													
$U_{-0}^{+,\mathrm{Im}}$	0.36	1.00												
$U_{-0}^{+,\mathrm{Re}}$	0.34	0.25	1.00											
U_-^-	0.19	0.06	0.03	1.00										
U_-^+	0.11	0.20	0.28	−0.13	1.00									
$U_{+0}^{-,\mathrm{Im}}$	0.07	0.22	−0.04	0.10	−0.16	1.00								
$U_{+0}^{-,\mathrm{Re}}$	−0.01	−0.08	−0.05	0.07	−0.05	0.32	1.00							
$U_{+0}^{+,\mathrm{Im}}$	0.22	0.56	0.17	−0.00	0.05	0.20	−0.25	1.00						
$U_{+0}^{+,\mathrm{Re}}$	0.08	0.23	0.02	0.11	−0.31	0.37	−0.06	0.41	1.00					
$U_{+-}^{-,\mathrm{Im}}$	−0.15	−0.20	−0.11	−0.27	−0.05	−0.15	−0.03	−0.12	−0.17	1.00				
$U_{+-}^{-,\mathrm{Re}}$	−0.12	−0.19	−0.21	0.08	0.02	−0.07	0.03	−0.16	−0.16	0.09	1.00			
$U_{+-}^{+,\mathrm{Im}}$	−0.22	−0.33	−0.35	0.06	−0.48	0.15	0.22	−0.33	0.12	0.10	0.12	1.00		
$U_{+-}^{+,\mathrm{Re}}$	0.03	−0.04	0.17	−0.02	0.10	−0.19	−0.19	0.05	−0.07	0.03	−0.15	−0.24	1.00	
U_+^-	−0.02	−0.03	−0.03	−0.07	0.11	0.14	0.30	−0.11	−0.11	0.18	0.20	0.02	−0.12	1.00

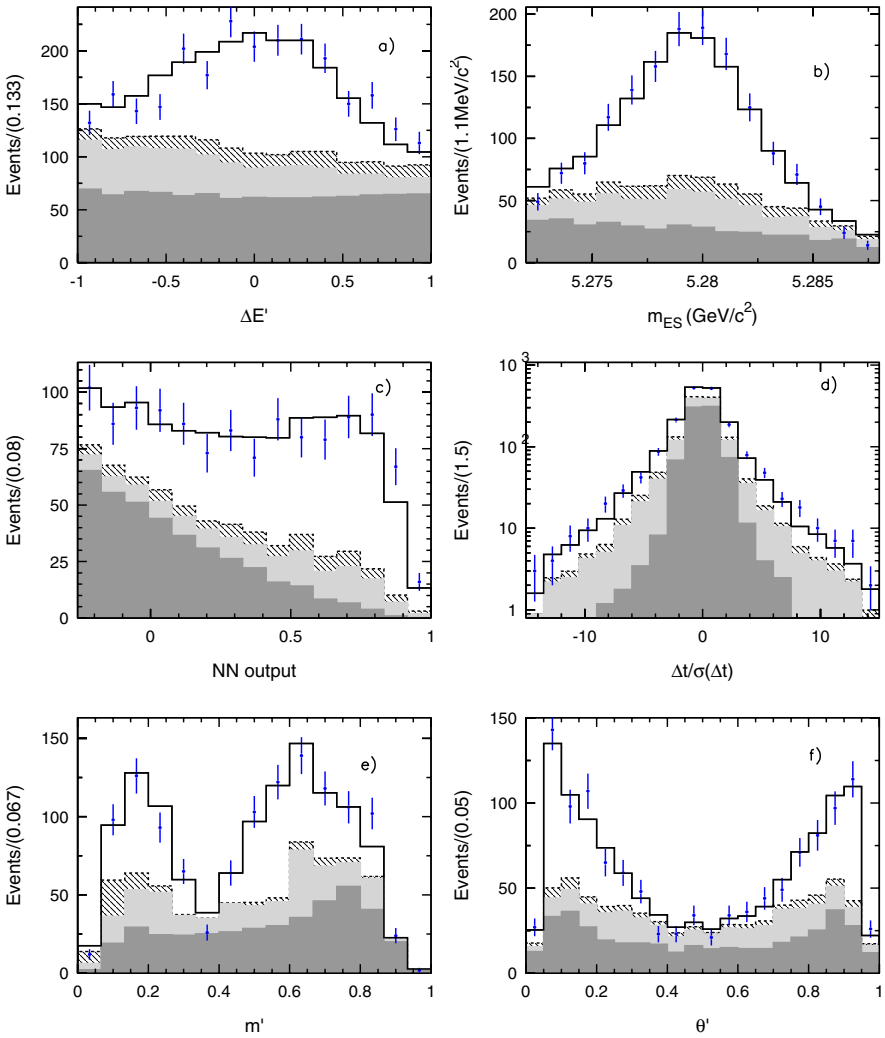

FIG. 4 (color online). Distributions of (a–f) $\Delta E'$, $m_{\rm ES}$, NN output, $\Delta t/\sigma(\Delta t)$, m', and θ' for samples enhanced in $B^0 \to \pi^+\pi^-\pi^0$ signal. The dots with error bars correspond to the on-resonance data. The solid histogram shows the projection of the fit result. The dark and light shaded areas represent the contribution from continuum and B-background events, respectively. The misreconstructed signal events are represented by the dashed histogram. The ratios of signal events over background events in the sample differs for each plot, but are typically $\sim$1.2.

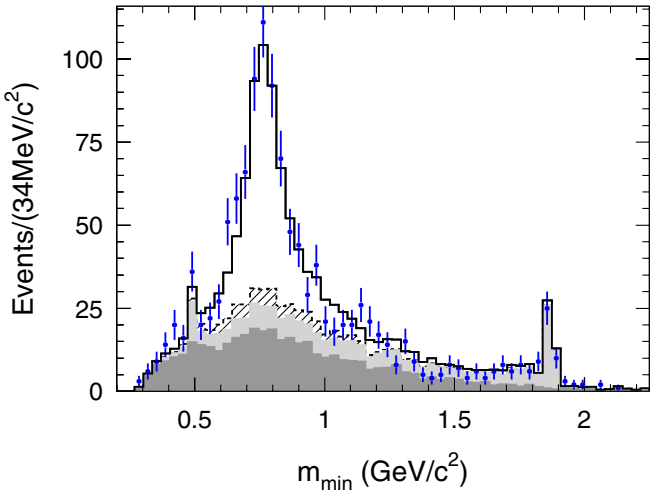

FIG. 5 (color online). Distribution of the minimum of the three di-pion invariant masses, for samples enhanced in $B^0 \to \pi^+\pi^-\pi^0$ signal. The dots with error bars correspond to the on-resonance data. The solid histogram shows the projection of the fit result. The dark and light shaded areas represent the contribution from continuum and B-background events, respectively. The misreconstructed signal events are represented by the dashed histogram. The peaks near 0.5 and 1.8 GeV/c^2 are from $B^0 \to K^0_s\pi^0$ and $B^0 \to D^+\pi^-$ decays, respectively.

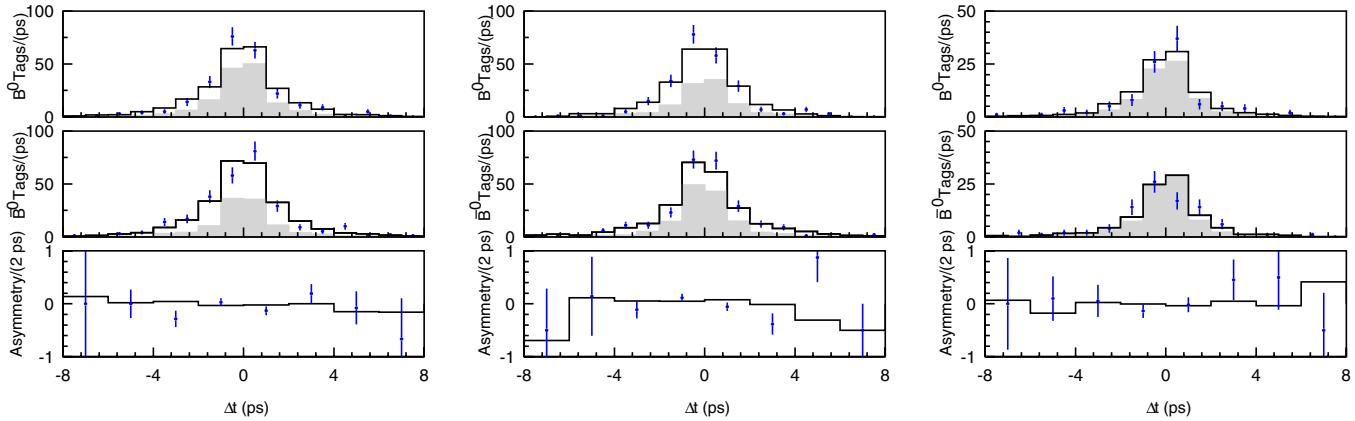

FIG. 6 (color online). The signal-enhanced Δt distributions in the ρ^+ (left), ρ^- (middle), and ρ^0 (right) dominated regions of the Dalitz plot for B^0 tags (top), $\bar{B}^0$ tags (middle), and the asymmetry between them (bottom). The dots with error bars correspond to the on-resonance data. The solid histogram shows the projection of the fit result. The shaded area represents the contribution from background events.

clearly that $\rho(770)$ dominates the signal component. Figure 6 shows the Δt distributions in the three ρ bands for B^0 and $\bar{B}^0$ tagged events, as well as their asymmetry.

V. SYSTEMATIC STUDIES

The contributions to the systematic error on the signal parameters are summarized in Table V. Table VI summarizes the correlation coefficients extracted from the systematic covariance matrix. For a given systematic effect, we vary a parameter in the fit (e.g. the $\rho(770)$ mass), refit the data, and construct the systematic covariance matrix for that source based on the deviations of the U and I coefficients from the nominal values. The (i, j) matrix element is given as

$$s_{i,j} \equiv \delta_i \delta_j, \tag{30}$$

where δ_i is the difference between the two fits for variable i. The total systematic covariance matrix is obtained by adding together the covariance matrices from the different systematic sources linearly.

To estimate the contribution to $B^0 \to \pi^+\pi^-\pi^0$ decay from other resonances and nonresonant decays, we fit the on-peak data including these other possible decays in the fit model. For simplicity, we assume a uniform Dalitz distribution for the nonresonant events and consider possible non-ρ resonances including $f_0(980)$, $f_2(1270)$, and a low mass S-wave σ whose mass and width we take to be 478 MeV/c^2 and 324 MeV/c^2, respectively [12]. The fit does not find a significant signal for any of those decays. However, the inclusion of the broad, low mass $\pi^+\pi^-$ S-wave component significantly degrades our ability to identify $\rho^0\pi^0$ events. The systematic effect (contained in the "Dalitz-plot model" rows in Table V) is estimated by generating Monte Carlo samples including the other $B^0 \to \pi^+\pi^-\pi^0$ modes and fitting with the nominal setup, where only $\rho(770)$ is taken into account.

We vary the mass and width of the $\rho(770)$, $\rho(1450)$, and $\rho(1700)$ resonances within ranges that exceed twice the errors found for these parameters extracted from τ decays and e^+e^- annihilations [13], and assign the observed shifts in the measured U and I coefficients as systematic uncertainties ("ρ, ρ', ρ'' line shape" in Table V). Since some of the U and I coefficients exhibit significant dependence on the $\rho(1450)$ and $\rho(1700)$ contributions, we leave their amplitudes (phases and fractions) free to vary in all fits.

To validate the fitting tool, we perform fits on large MC samples with the measured proportions of signal, continuum, and B-background events. No significant biases are observed in these fits. The statistical uncertainties on their fit parameters are taken as systematic uncertainties ("Fit bias" in Table V).

Another potentially large source of systematic uncertainty is the B-background model. The expected event yields from the background modes are varied according to the uncertainties in the measured or estimated branching fractions ("$N_{\mathrm{Background}}$" in Table V). Since B-background modes may exhibit CP violation, the corresponding parameters are varied either within their measured ranges (if available) or within ± 0.5 (if unmeasured) ("B background CP" in Table V). We also have calculated the effects of tag side interference on the U and I coefficients and have included them in the table.

Other systematic effects are much less important to the measurements of U and I coefficients and are combined in the "Others" field in Table V. Details are given below.

The parameters for the continuum events are determined by the fit. No additional systematic uncertainties are assigned to them. An exception to this is the Dalitz-plot PDF; to estimate the systematic uncertainty from the m_{ES} sideband extrapolation, we select large samples of off-

TABLE V. Summary of systematic uncertainties.

	I_0	I_-	I_{-0}^{Im}	I_{-0}^{Re}	I_+	I_{+0}^{Im}
Dalitz-plot model	0.010	0.006	0.110	0.102	0.020	0.018
ρ, ρ', ρ'' line shape	0.003	0.012	0.240	0.103	0.009	0.225
Fit bias	0.000	0.002	0.012	0.049	0.005	0.015
$N_{\mathrm{background}}$	0.005	0.005	0.072	0.096	0.005	0.045
B-background CP	0.004	0.013	0.064	0.083	0.009	0.050
Tag side interference	0.000	0.003	0.018	0.006	0.011	0.003
Others	0.002	0.007	0.077	0.059	0.005	0.065
Total	0.012	0.022	0.292	0.207	0.027	0.245

	I_{+0}^{Re}	I_{+-}^{Im}	I_{+-}^{Re}	U_0^-	U_0^+	$U_{-0}^{-,\mathrm{Im}}$	$U_{-0}^{-,\mathrm{Re}}$
Dalitz-plot model	0.017	0.007	0.127	0.082	0.041	0.144	0.209
ρ, ρ', ρ'' line shape	0.308	0.138	0.306	0.012	0.012	0.086	0.159
Fit bias	0.093	0.014	0.239	0.007	0.001	0.120	0.145
$N_{\mathrm{background}}$	0.207	0.221	0.496	0.007	0.010	0.037	0.082
B-background CP	0.121	0.168	0.088	0.015	0.005	0.052	0.044
Tag side interference	0.019	0.033	0.026	0.000	0.001	0.007	0.022
Others	0.092	0.133	0.078	0.004	0.004	0.016	0.046
Total	0.413	0.339	0.653	0.085	0.044	0.216	0.318

	$U_{-0}^{+,\mathrm{Im}}$	$U_{-0}^{+,\mathrm{Re}}$	U_-^-	U_-^+	$U_{+0}^{-,\mathrm{Im}}$	$U_{+0}^{-,\mathrm{Re}}$	$U_{+0}^{+,\mathrm{Im}}$
Dalitz-plot model	0.034	0.024	0.022	0.030	0.036	0.258	0.076
ρ, ρ', ρ'' line shape	0.222	0.045	0.010	0.030	0.050	0.216	0.089
Fit bias	0.010	0.023	0.001	0.007	0.214	0.038	0.001
$N_{\mathrm{background}}$	0.038	0.051	0.020	0.009	0.080	0.073	0.051
B-background CP	0.038	0.015	0.041	0.014	0.073	0.052	0.042
Tag side interference	0.022	0.012	0.004	0.003	0.028	0.004	0.001
Others	0.011	0.007	0.015	0.010	0.038	0.037	0.032
Total	0.233	0.079	0.054	0.048	0.252	0.353	0.138

	$U_{+0}^{+,\mathrm{Re}}$	$U_{+-}^{-,\mathrm{Im}}$	$U_{+-}^{-,\mathrm{Re}}$	$U_{+-}^{+,\mathrm{Im}}$	$U_{+-}^{+,\mathrm{Re}}$	U_+^-
Dalitz-plot model	0.045	0.014	0.250	0.703	0.227	0.010
ρ, ρ', ρ'' line shape	0.140	0.169	0.200	0.169	0.159	0.031
Fit bias	0.003	0.130	0.001	0.010	0.035	0.007
$N_{\mathrm{background}}$	0.106	0.288	0.114	0.099	0.083	0.016
B-background CP	0.059	0.055	0.238	0.028	0.038	0.036
Tag side interference	0.031	0.031	0.044	0.031	0.028	0.007
Others	0.060	0.045	0.112	0.012	0.079	0.009
Total	0.202	0.367	0.432	0.731	0.306	0.054

	$\mathcal{A}_{\rho\pi}$	C	ΔC	S	ΔS	$C_{\rho\pi}^{00}$	$S_{\rho\pi}^{00}$	$f(\rho^0\pi^0)$
Dalitz-plot model	0.008	0.002	0.013	0.015	0.024	0.464	0.130	0.037
ρ, ρ', ρ'' line shape	0.011	0.021	0.011	0.016	0.008	0.048	0.020	0.007
Fit bias	0.015	0.026	0.081	0.024	0.055	0.236	0.062	0.004
$N_{\mathrm{background}}$	0.003	0.004	0.014	0.005	0.008	0.030	0.036	0.005
B-background CP	0.005	0.032	0.006	0.018	0.007	0.059	0.028	0.002
Tag side interference	0.001	0.002	0.006	0.009	0.013	0.016	0.018	0.001
Others	0.003	0.007	0.006	0.006	0.008	0.017	0.014	0.002
Total	0.021	0.047	0.085	0.039	0.063	0.527	0.188	0.039

TABLE VI. Correlation matrix of systematic uncertainties for the U and I coefficients. Since the matrix is symmetric, all elements above the diagonal are omitted.

	$N_{3\pi}$	I_0	I_-	I_{-0}^{Im}	I_{-0}^{Re}	I_+	I_{+0}^{Im}	I_{+0}^{Re}	I_{+-}^{Im}	I_{+-}^{Re}	U_0^-	U_0^+	$U_{-0}^{-,\mathrm{Im}}$
$N_{3\pi}$	1.00												
I_0	0.10	1.00											
I_-	0.07	−0.20	1.00										
I_{-0}^{Im}	0.00	−0.32	0.78	1.00									
I_{-0}^{Re}	0.29	0.17	−0.52	−0.56	1.00								
I_+	−0.12	0.48	−0.01	−0.18	0.29	1.00							
I_{+0}^{Im}	−0.07	−0.25	0.57	0.70	−0.25	0.27	1.00						
I_{+0}^{Re}	0.20	0.36	−0.21	−0.09	−0.10	−0.48	−0.58	1.00					
I_{+-}^{Im}	−0.03	−0.35	−0.33	−0.14	0.36	0.23	0.31	−0.55	1.00				
I_{+-}^{Re}	0.36	0.55	0.01	0.13	−0.20	−0.17	−0.18	0.75	−0.54	1.00			
U_0^-	0.01	0.90	−0.30	−0.39	0.39	0.66	−0.14	0.09	−0.07	0.27	1.00		
U_0^+	−0.11	−0.75	0.46	0.58	−0.55	−0.65	0.22	0.04	−0.14	−0.12	−0.89	1.00	
$U_{-0}^{-,\mathrm{Im}}$	0.49	−0.66	0.28	0.34	−0.11	−0.44	0.29	−0.17	0.25	−0.20	−0.73	0.62	1.00
$U_{-0}^{-,\mathrm{Re}}$	−0.39	0.53	−0.50	−0.55	0.35	0.53	−0.24	0.03	0.26	−0.08	0.71	−0.71	−0.76
$U_{-0}^{+,\mathrm{Im}}$	−0.07	0.15	−0.39	−0.49	−0.22	−0.29	−0.54	0.49	−0.18	0.16	−0.00	−0.05	−0.11
$U_{-0}^{+,\mathrm{Re}}$	−0.30	−0.57	0.26	0.11	−0.04	0.08	0.36	−0.75	0.34	−0.84	−0.38	0.26	0.28
U_-^-	−0.05	−0.44	−0.25	−0.22	0.14	−0.24	−0.14	−0.11	0.46	−0.34	−0.38	0.24	0.36
U_-^+	−0.10	0.75	−0.24	−0.35	0.04	0.33	−0.26	0.39	−0.23	0.33	0.74	−0.61	−0.67
$U_{+0}^{-,\mathrm{Im}}$	0.87	0.07	−0.10	−0.18	0.50	−0.04	−0.15	0.14	0.18	0.10	0.06	−0.19	0.48
$U_{+0}^{-,\mathrm{Re}}$	−0.18	−0.50	−0.00	0.00	−0.41	−0.68	−0.38	0.35	−0.14	−0.12	−0.62	0.59	0.24
$U_{+0}^{+,\mathrm{Im}}$	−0.05	−0.50	−0.09	−0.01	−0.19	−0.25	0.16	−0.27	0.18	−0.18	−0.59	0.40	0.52
$U_{+0}^{+,\mathrm{Re}}$	0.03	−0.22	−0.06	−0.09	0.51	0.44	0.34	−0.79	0.65	−0.58	0.05	−0.24	0.14
$U_{+-}^{-,\mathrm{Im}}$	0.33	0.19	0.26	0.46	−0.27	−0.07	0.28	0.25	−0.33	0.64	−0.05	0.17	0.24
$U_{+-}^{-,\mathrm{Re}}$	0.05	0.62	0.26	0.22	−0.04	0.29	0.14	0.26	−0.43	0.43	0.61	−0.38	−0.55
$U_{+-}^{+,\mathrm{Im}}$	−0.08	−0.84	0.26	0.34	−0.50	−0.64	0.14	−0.09	0.11	−0.33	−0.94	0.86	0.72
$U_{+-}^{+,\mathrm{Re}}$	−0.04	0.62	0.13	0.08	0.20	0.62	0.27	−0.20	−0.21	0.16	0.69	−0.54	−0.49
U_+^-	0.14	0.39	−0.33	−0.33	0.11	−0.06	−0.40	053	−0.06	0.36	0.31	−0.25	−0.15

	$U_{-0}^{-,\mathrm{Re}}$	$U_{-0}^{+,\mathrm{Im}}$	$U_{-0}^{+,\mathrm{Re}}$	U_-^-	U_-^+	$U_{+0}^{-,\mathrm{Im}}$	$U_{+0}^{-,\mathrm{Re}}$	$U_{+0}^{+,\mathrm{Im}}$	$U_{+0}^{+,\mathrm{Re}}$	$U_{+-}^{-,\mathrm{Im}}$	$U_{+-}^{-,\mathrm{Re}}$	$U_{+-}^{+,\mathrm{Im}}$	$U_{+-}^{+,\mathrm{Re}}$	U_+^-
$U_{-0}^{-,\mathrm{Re}}$	1.00													
$U_{-0}^{+,\mathrm{Im}}$	0.29	1.00												
$U_{-0}^{+,\mathrm{Re}}$	−0.13	−0.27	1.00											
U_-^-	−0.04	0.12	0.17	1.00										
U_-^+	0.72	0.51	−0.39	−0.41	1.00									
$U_{+0}^{-,\mathrm{Im}}$	−0.17	−0.04	−0.13	0.15	−0.06	1.00								
$U_{+0}^{-,\mathrm{Re}}$	−0.14	0.57	0.15	0.37	−0.09	−0.12	1.00							
$U_{+0}^{+,\mathrm{Im}}$	−0.46	0.13	0.19	0.28	−0.57	−0.13	0.11	1.00						
$U_{+0}^{+,\mathrm{Re}}$	0.04	−0.64	0.54	0.23	−0.45	0.21	−0.52	0.13	1.00					
$U_{+-}^{-,\mathrm{Im}}$	−0.54	−0.29	−0.45	−0.28	−0.23	0.08	−0.39	0.28	−0.15	1.00				
$U_{+-}^{-,\mathrm{Re}}$	0.29	−0.11	−0.34	−0.73	0.63	−0.10	−0.36	−0.68	−0.33	0.11	1.00			
$U_{+-}^{+,\mathrm{Im}}$	−0.59	0.19	0.41	0.41	−0.59	−0.10	0.73	0.57	−0.16	−0.06	−0.62	1.00		
$U_{+-}^{+,\mathrm{Re}}$	0.21	−0.52	−0.05	−0.54	0.30	−0.07	−0.81	−0.39	0.29	0.31	0.58	−0.77	1.00	
U_+^-	0.35	0.44	−0.49	0.36	0.44	0.23	0.17	−0.22	−0.38	−0.03	−0.01	−0.20	−0.15	1.00

resonance data by loosening the requirements on ΔE and the NN. We compare the distributions of m' and θ' between the $m_{\rm ES}$ sideband and the signal region. No significant differences are found. We assign as systematic error the effect seen when weighting the continuum Dalitz-plot PDF by the ratio of the 2-dimensional histograms taken from the signal region and sideband data sets. This effect is mostly statistical in origin.

The uncertainties associated with Δm_d and τ are estimated by varying these parameters within the uncertainties on the world averages [12].

The systematic effects due to the signal PDFs comprise uncertainties in the PDF parametrization, the treatment of misreconstructed decays, the tagging performance, and the modeling of the signal contributions.

When the signal PDFs are determined from fits to a control sample of fully reconstructed B decays to exclusive final states with charm, the uncertainties are obtained by varying the parameters within the statistical uncertainties. In other cases, the dominant parameters have been left free to vary in the fit, and the differences observed in these fits are taken as systematic errors.

The average fraction of misreconstructed signal events predicted by the MC simulation has been verified with fully reconstructed $B \to D\rho$ events [17]. No significant differences between data and the simulation are found. We vary $\bar{f}_{\rm SCF}$ for all tagging categories relatively by 25% to estimate the systematic uncertainty.

As is done for the signal PDFs, we vary the Δt resolution parameters and the flavor-tagging parameters within their uncertainties and assign the differences observed in the data fit with respect to the nominal fit as systematic errors.

The systematic errors for the parameters that measure interference effects are dominated by the uncertainty in the signal model, mainly the description of the ρ resonance tails. For the other parameters, the uncertainty on the fit bias and the B-background contamination are important.

As a validation of our treatment of the time dependence we allow τ_{B^0} to vary in the fit. We find $\tau_{B^0} = (1.513 \pm 0.066)$ ps, while the remaining free parameters are consistent with the nominal fit. To validate the SCF modeling, we leave the average SCF fractions per tagging category free to vary in the fit and find results that are consistent with the MC prediction.

VI. INTERPRETATION OF THE RESULTS

We can use the results of this time-dependent Dalitz analysis to extract the $B^0(\bar{B}^0) \to \rho^\pm\pi^\mp$ parameters defined in Ref. [17]:

$$f^{\rho^\pm\pi^\mp}_{Q_{\rm tag}}(\Delta t) = (1 \pm \mathcal{A}_{\rho\pi})\frac{e^{-|\Delta t|/\tau}}{4\tau}[1 + Q_{\rm tag}(S \pm \Delta S) \times \sin(\Delta m_d \Delta t) - Q_{\rm tag}(C \pm \Delta C) \times \cos(\Delta m_d \Delta t)], \quad (31)$$

where $Q_{\rm tag} = 1(-1)$ when the tagging meson $B^0_{\rm tag}$ is a $B^0(\bar{B}^0)$. The time- and flavor-integrated charge asymmetry $\mathcal{A}_{\rho\pi}$ measures direct CP violation and the quantities S and C parametrize mixing-induced CP violation related to the angle α, and flavor-dependent direct CP violation, respectively.

The U and I coefficients are related to the parameters as follows:

$$C^+ = \frac{U^-_+}{U^+_+}, \qquad C^- = \frac{U^-_-}{U^+_-}, \qquad S^+ = \frac{2I_+}{U^+_+}, \qquad S^- = \frac{2I_-}{U^+_-}, \qquad \mathcal{A}_{\rho\pi} = \frac{U^+_+ - U^+_-}{U^+_+ + U^+_-}, \quad (32)$$

where $C = (C^+ + C^-)/2$, $\Delta C = (C^+ - C^-)/2$, $S = (S^+ + S^-)/2$, and $\Delta S = (S^+ - S^-)/2$. The definitions of Eq. (32) explicitly account for the presence of interference effects, and are thus exact even for a ρ with finite width, as long as the U and I coefficients are obtained with a Dalitz-plot analysis. This treatment leads to slightly increased statistical uncertainties compared to the results obtained neglecting the interference effects.

Using a least-squares method including statistical and systematic correlations for the U and I coefficients, we obtain:

$$\mathcal{A}_{\rho\pi} = -0.14 \pm 0.05 \pm 0.02, \quad (33)$$

$$C = 0.15 \pm 0.09 \pm 0.05, \quad (34)$$

$$S = -0.03 \pm 0.11 \pm 0.04, \quad (35)$$

where the first errors are statistical and the second are the systematic uncertainties. For the other parameters in the description of the $B^0(\bar{B}^0) \to \rho\pi$ decay-time dependence, we measure

$$\Delta C = 0.39 \pm 0.09 \pm 0.09, \quad (36)$$

$$\Delta S = -0.01 \pm 0.14 \pm 0.06. \quad (37)$$

In addition, we measure the $B^0 \to \rho^0\pi^0$ CP-violation parameters and decay fraction to be

$$C_{00} = \frac{U^-_0}{U^+_0} = -0.10 \pm 0.40 \pm 0.53, \quad (38)$$

$$S_{00} = \frac{2I_0}{U^+_0} = 0.04 \pm 0.44 \pm 0.18, \quad (39)$$

$$f_{00} = \frac{U^+_0}{U^+_+ + U^+_- + U^+_0} = 0.136 \pm 0.036 \pm 0.039. \quad (40)$$

The systematic errors are dominated by the uncertainty on the CP content of the B-related backgrounds. Other contributions are the signal description in the likelihood model (including the limit on nonresonant $B^0 \to \pi^+\pi^-\pi^0$ events), and the fit bias uncertainty. The large systematic

TABLE VII. Correlation matrix of the quasi-two-body parameters.

	$\mathcal{A}_{\rho\pi}$	$\mathfrak{C}$	ΔC	$\mathfrak{S}$	ΔS	$C^{00}_{\rho\pi}$	$S^{00}_{\rho\pi}$	$f(\rho^0\pi^0)$
$\mathcal{A}_{\rho\pi}$	1.00							
$\mathfrak{C}$	−0.06	1.00						
ΔC	0.12	0.38	1.00					
$\mathfrak{S}$	−0.07	−0.13	−0.15	1.00				
ΔS	−0.04	−0.12	−0.26	0.33	1.00			
$\mathfrak{C}_{00}$	−0.38	−0.15	−0.18	0.19	0.22	1.00		
$\mathfrak{S}_{00}$	−0.24	0.18	0.50	−0.18	−0.14	0.35	1.00	
f_{00}	0.19	−0.04	−0.09	−0.17	−0.38	−0.84	−0.70	1.00

error on C_{00} is due to the possible $\pi^+\pi^-$ S-wave contribution. The correlation matrix, including statistical and systematic uncertainties, of the eight quasi-two-body parameters is given in Table VII.

One can transform the experimentally convenient (uncorrelated) direct-CP violation parameters C and $\mathcal{A}_{\rho\pi}$ into $\mathcal{A}^{+-}_{\rho\pi}$, $\mathcal{A}^{-+}_{\rho\pi}$, defined by

$$\mathcal{A}^{+-}_{\rho\pi} = \frac{|\kappa^{+-}|^2 - 1}{|\kappa^{+-}|^2 + 1} = -\frac{\mathcal{A}_{\rho\pi} + C + \mathcal{A}_{\rho\pi}\Delta C}{1 + \Delta C + \mathcal{A}_{\rho\pi} C},$$
$$\mathcal{A}^{-+}_{\rho\pi} = \frac{|\kappa^{-+}|^2 - 1}{|\kappa^{-+}|^2 + 1} = \frac{\mathcal{A}_{\rho\pi} - C - \mathcal{A}_{\rho\pi}\Delta C}{1 - \Delta C - \mathcal{A}_{\rho\pi} C}, \quad (41)$$

where $\kappa^{+-} = (q/p)\bar{A}^-/A^+$ and $\kappa^{-+} = (q/p)\bar{A}^+/A^-$, so that $\mathcal{A}^{+-}_{\rho\pi}$ ($\mathcal{A}^{-+}_{\rho\pi}$) involves only diagrams where the ρ (π) meson is formed from the W boson. We find

$$\mathcal{A}^{+-}_{\rho\pi} = 0.03 \pm 0.07 \pm 0.04, \quad (42)$$

$$\mathcal{A}^{-+}_{\rho\pi} = -0.37 \pm 0.16^{+0.09}_{-0.10}, \quad (43)$$

with a correlation coefficient of 0.62 between $\mathcal{A}^{+-}_{\rho\pi}$ and $\mathcal{A}^{-+}_{\rho\pi}$. The confidence level contours including systematic uncertainties are shown in Fig. 7. The significance, including systematic uncertainties and calculated by using a minimum χ^2 method, of direct CP violation is less than 3.0σ.

The measurement of the resonance interference terms allows us to determine the relative phase

$$\delta_{+-} = \arg(A^{+*}A^-) \quad (44)$$

between the amplitudes of the decays $B^0 \to \rho^-\pi^+$ and $B^0 \to \rho^+\pi^-$. Through the definitions in Eqs. (9)–(14), we can derive a constraint on δ_{+-} from the measured U and I coefficients by performing a least-squares minimization with the six complex amplitudes as free parameters. The constraint can be improved with the use of strong isospin symmetry. The amplitudes A^κ represent the sum of tree-level and penguin-type amplitudes, which have different CKM factors: the tree-level (T^κ) $B^0 \to \rho^\kappa\pi^{\bar{\kappa}}$ transition amplitude is proportional to $V_{ud}V^*_{ub}$, while the corresponding penguin-type amplitude (P^κ) involves $V_{qd}V^*_{qb}$, where $q = u, c, t$. Here we denote by $\bar{\kappa}$ the charge conjugate of κ, where $\bar{\kappa} = 0$ when $\kappa = 0$. Using the unitarity of the CKM matrix one can reorganize the amplitudes and obtain [14]

$$A^\kappa = T^\kappa e^{-i\alpha} + P^\kappa, \qquad (q/p)\bar{A}^\kappa = T^{\bar{\kappa}} e^{+i\alpha} + P^{\bar{\kappa}}, \quad (45)$$

where the magnitudes of the CKM factors have been absorbed in T^κ, P^κ, $T^{\bar{\kappa}}$, and $P^{\bar{\kappa}}$. The Eqs. (45) represent 13 unknowns of which two can be fixed due to an arbitrary global phase and the normalization condition $U^+_+ = 1$. Using strong isospin symmetry one can identify $P^0 = -(P^+ + P^-)/2$, which reduces the number of unknowns to be determined by the fit to nine. This set of parameters provides the constraint on δ_{+-}, shown in the left plot of Fig. 8. We find for the solution that is favored by the fit

$$\delta_{+-} = (37 \pm 37)^\circ, \quad (46)$$

where the errors include both statistical and systematic effects. There is only a marginal constraint on δ_{+-} obtained at 95% confidence level (C.L.).

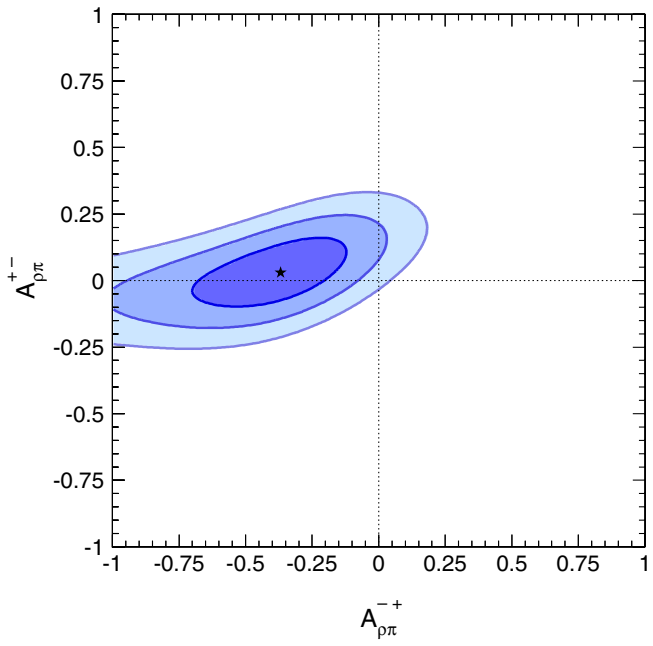

FIG. 7 (color online). Confidence level contours for the direct CP asymmetries $\mathcal{A}^{+-}_{\rho\pi}$ versus $\mathcal{A}^{-+}_{\rho\pi}$. The shaded areas represent 1σ, 2σ, and 3σ contours, respectively.

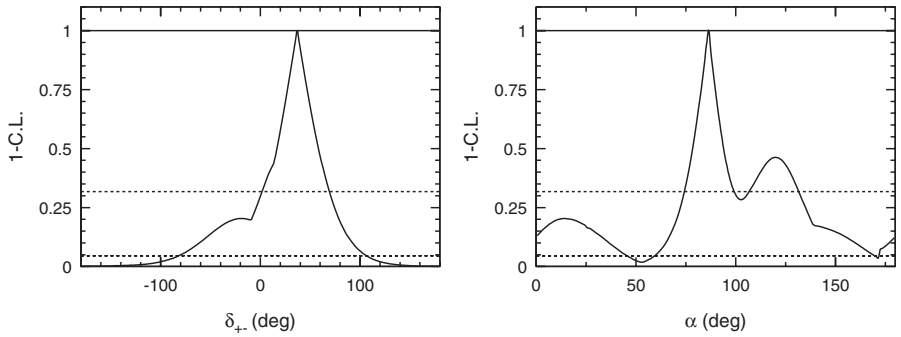

FIG. 8. Confidence level functions for δ_{+-} (left) and α (right). Indicated by the dashed horizontal lines are the confidence level (C.L.) values corresponding to 1σ and 2σ, respectively.

Finally, following the same procedure, we can also derive a constraint on α from the measured U and I coefficients. The resulting C.L. function versus α is given in the right-hand plot of Fig. 8, including systematic uncertainties. Ignoring the mirror solution at $\alpha + 180°$, we find at 68% C.L.

$$\alpha = (87^{+45}_{-13})°. \tag{47}$$

Almost no constraint on α is achieved at two sigma and beyond.

VII. SUMMARY

We have presented a measurement of CP-violating asymmetries in $B^0 \to \pi^+\pi^-\pi^0$ decays dominated by the ρ resonance. The results are obtained from a data sample of 375×10^6 $\Upsilon(4S) \to B\bar{B}$ decays. We perform a time-dependent Dalitz-plot analysis. From the measurement of the coefficients of 26 form-factor bilinears we determine the three CP-violating and two CP-conserving quasi-two-body parameters, and find no evidence of direct CP violation. Taking advantage of the interference between the ρ resonances in the Dalitz plot, we derive constraints on the relative strong phase between B^0 decays to $\rho^+\pi^-$ and $\rho^-\pi^+$, and on the angle α of the unitarity triangle. These measurements are consistent with the results obtained by Belle [27] as well as with the expectation of a SM fit to all constraints on the CKM matrix [28,29].

ACKNOWLEDGMENTS

We are grateful for the extraordinary contributions of our PEP-II colleagues in achieving the excellent luminosity and machine conditions that have made this work possible. The success of this project also relies critically on the expertise and dedication of the computing organizations that support *BABAR*. The collaborating institutions wish to thank SLAC for its support and the kind hospitality extended to them. This work is supported by the U.S. Department of Energy and National Science Foundation, the Natural Sciences and Engineering Research Council (Canada), Institute of High Energy Physics (China), the Commissariat à l'Energie Atomique and Institut National de Physique Nucléaire et de Physique des Particules (France), the Bundesministerium für Bildung und Forschung and Deutsche Forschungsgemeinschaft (Germany), the Istituto Nazionale di Fisica Nucleare (Italy), the Foundation for Fundamental Research on Matter (The Netherlands), the Research Council of Norway, the Ministry of Science and Technology of the Russian Federation, Ministerio de Educación y Ciencia (Spain), and the Particle Physics and Astronomy Research Council (United Kingdom). Individuals have received support from the Marie-Curie IEF program (European Union) and the A. P. Sloan Foundation.

[1] B. Aubert *et al.* (*BABAR* Collaboration), Phys. Rev. Lett. **94**, 161803 (2005).
[2] K. F. Chen *et al.* (Belle Collaboration), Phys. Rev. Lett. **98**, 031802 (2007).
[3] N. Cabibbo, Phys. Rev. Lett. **10**, 531 (1963); M. Kobayashi and T. Maskawa, Prog. Theor. Phys. **49**, 652 (1973).
[4] Charge conjugate decay modes are assumed unless explicitly stated.
[5] B. Aubert *et al.* (*BABAR* Collaboration), Phys. Rev. Lett. **95**, 151803 (2005).
[6] K. Abe *et al.* (Belle Collaboration), Phys. Rev. Lett. **95**, 101801 (2005).
[7] B. Aubert *et al.* (*BABAR* Collaboration), Phys. Rev. Lett. **95**, 041805 (2005).
[8] K. Abe *et al.* (Belle Collaboration), Phys. Rev. Lett. **97**, 171801 (2006).
[9] M. Gronau and D. London, Phys. Rev. Lett. **65**, 3381

(1990).
[10] H. J. Lipkin, Y. Nir, H. R. Quinn, and A. Snyder, Phys. Rev. D **44**, 1454 (1991).
[11] H. R. Quinn and A. E. Snyder, Phys. Rev. D **48**, 2139 (1993).
[12] S. Eidelman *et al.* (Particle Data Group), Phys. Lett. B **592**, 1 (2004).
[13] R. Barate *et al.* (ALEPH Collaboration), Z. Phys. C **76**, 15 (1997); we use updated line shape fits including new data from e^+e^- annihilation [30] and τ spectral functions [31] (masses and widths in MeV/c^2): $m_{\rho^\pm(770)} = 775.5 \pm 0.6$, $m_{\rho^0(770)} = 773.1 \pm 0.5$, $\Gamma_{\rho^\pm(770)} = 148.2 \pm 0.8$, $\Gamma_{\rho^0(770)} = 148.0 \pm 0.9$, $m_{\rho(1450)} = 1409 \pm 12$, $\Gamma_{\rho(1450)} = 500 \pm 37$, $m_{\rho(1700)} = 1749 \pm 20$, and $\Gamma_{\rho(1700)} \equiv 235$.
[14] The *BABAR* Physics Book, edited by P. F. Harrison and H. R. Quinn, Report No. SLAC-R-504, 1998.
[15] G. J. Gounaris and J. J. Sakurai, Phys. Rev. Lett. **21**, 244 (1968).
[16] H. R. Quinn and J. Silva, Phys. Rev. D **62**, 054002 (2000).
[17] B. Aubert *et al.* (*BABAR* Collaboration), Phys. Rev. Lett. **91**, 201802 (2003).
[18] S. Agostinelli *et al.* (GEANT4 Collaboration), Nucl. Instrum. Methods Phys. Res., Sect. A **506**, 250 (2003).
[19] B. Aubert *et al.* (*BABAR* Collaboration), Nucl. Instrum. Methods Phys. Res., Sect. A **479**, 1 (2002).
[20] P. Gay, B. Michel, J. Proriol, and O. Deschamps, "Tagging Higgs Bosons in Hadronic LEP-2 Events with Neural Networks," in Pisa 1995, New Computing Techniques in Physics Research (1995), p. 725.
[21] K. Anikeev *et al.* (Heavy Flavor Averaging Group), arXiv:hep-ex/0505100.
[22] T. Skwarnicki, Report No. DESY F31-86-02, Ph.D. thesis, DESY, 1986; see also Ref. [1].
[23] K. S. Cranmer, Comput. Phys. Commun. **136**, 198 (2001).
[24] H. Albrecht *et al.* (ARGUS Collaboration), Z. Phys. C **48**, 543 (1990).
[25] B. Aubert *et al.* (*BABAR* Collaboration), Phys. Rev. Lett. **93**, 051802 (2004).
[26] J. Dragic *et al.* (Belle Collaboration), Phys. Rev. D **73**, 111105 (2006).
[27] A. Kusaka *et al.* (Belle Collaboration), Phys. Rev. Lett. **98**, 221602 (2007).
[28] J. Charles *et al.*, Eur. Phys. J. C **41**, 1 (2005).
[29] M. Bona *et al.*, J. High Energy Phys. 07 (2005) 028.
[30] R. R. Akhmetshin *et al.* (CMD-2 Collaboration), Phys. Lett. B **527**, 161 (2002).
[31] S. Schael *et al.* (ALEPH Collaboration), Phys. Rep. **421**, 191 (2005).